Cosmological Signatures in Galaxy Cluster Structures

by

James J. Frederic

Submitted to the Department of Physics
in partial fulfillment of the requirements for the degree of

Doctor of Philosophy

at the

MASSACHUSETTS INSTITUTE OF TECHNOLOGY

January 1997

Author .....
Department of Physics
January 13, 1997

Certified by .....
Edmund Bertschinger
Associate Professor
Thesis Supervisor

Accepted by .....
George F. Koster
Chairman, Graduate Committee

Cosmological Signatures in Galaxy Cluster Structures

by

James J. Frederic

Submitted to the Department of Physics
on January 13, 1997, in partial fulfillment of the
requirements for the degree of
Doctor of Philosophy

Abstract

We study substructure in X-ray clusters of galaxies by application of a set of statistics, the power ratios of Buote & Tsai (1995), to a simulated cluster and in the context of a simple analytic model for merger events. The simulation involves a newly developed code for performing high resolution gravity and gas dynamics simulations in cosmological volumes.

Thesis Supervisor: Edmund Bertschinger
Title: Associate Professor

Acknowledgments

I am grateful to my advisor, Ed Bertschinger, for all his support: scientific, professional, financial, and even moral. Ed's encouragement and confidence in my ability provided me a needed and much appreciated pick me up on many occasions.

As I finally leave the role of student, formally at least, I wish to thank my parents, Wayne and Rosemary Frederic, for putting me on this path and encouraging me along it. As a parent myself now I realize more each day the sacrifices they made to make me who I am. Each night when I return from work (too late), my frustrations melt away in the excited greeting of my young son Ethan. My greatest hope for my relationship with him is that when he is a man he is still as happy to see me as I am to see my parents.

All the long days, nights and weekends that went into this thesis place me deep in debt to my wife Tonya. Tonya, I.O.U. one year of parenting. Thanks for shouldering more than your share of the home burdens while I worked, for being a great mother to Ethan, for all your love.

Thanks to Ethan, my little buddy. Without understanding how or why, you make any burden tolerable, and you make me happy.

And to the next little Frederic, due any minute now, thanks for waiting. Daddy's ready now.

Contents

Chapter 1

Introduction

There are many ways in which galaxy clusters may reflect cosmological parameters. For example, the normalization and shape of the cluster luminosity function certainly reflect the amplitude and shape of the power spectrum of initial density fluctuations. Assuming that the ratio of baryonic to total mass in large clusters is the universal ratio, measured baryon fractions can be combined with nucleosynthesis constraints on the overall baryon density to infer the total mass density Ω (White et al. 1993). Measurement of the Sunyaev-Zel'dovich effect in clusters can be used to determine the cluster's true size and hence its distance, bypassing the many rungs in the cosmological distance ladder and allowing determination of the Hubble parameter H_0.

The internal structure of clusters of galaxies may be a powerful discriminator of cosmological models as well. In particular, the amount of substructure in clusters is expected to be highly sensitive to the mean density of the universe (Richstone et al. 1992). Assuming that mergers and accretions onto clusters impart internal structure to the clusters and that such structure is then erased via relaxation processes, the amount of substructure surviving today is a measure of the epoch of cluster formation. More substructure indicates more recent cluster formation and a higher mean matter density. This approach has been taken theoretically by Richstone et al. (1992), Lacey & Cole (1993, 1994), and Kaufmann & White (1993). Each of these authors applied extensions of the Press & Schechter (1974) formalism to study the fraction of clusters which have recently formed. By assuming some value for the survival time

of substructure, and by estimating the fraction of clusters which currently possess substructure, Richstone et al. (1992) and Lacey & Cole (1993) determined that the frequency of substructure present in available data favors a large value for the mean mass density of the universe, $\Omega \geq 0.5$. Kauffmann & White (1993) reached no conclusion in this regard, as the survival time of substructure is so uncertain. Other cosmological parameters, such as the power spectrum and cosmological constant, may also leave a measurable signature in cluster structures (Richstone et al. 1992, Lacey & Cole 1993).

The issue of substructure survival time lends itself naturally to testing by simulation. Nakamura et al. (1995) and McGlynn & Fabian (1984) have addressed this issue directly, albeit with simple models of equal mass subclusters, without gas, and not in a cosmological setting. Taking the substructure survival time to be the time from the initial encounter until only a single density peak remains, they find that this timescale is very sensitive to the assumed mass profiles and velocity dispersions of the subclusters, as well as the initial conditions for the orbit. Other simulators, including Crone et al. (1994), Evrard et al. (1993), Mohr et al. (1995), Buote & Tsai (1995), and Buote & Xu (1996) have taken a different approach: simulating clusters in different cosmological models in order to establish the model discriminating power of their structure statistics. In addition, Mohr et al. (1993, 1995) compared the substructure measured in the simulated clusters to that in data from the Einstein observatory, while Buote & Tsai (1996) and Tsai & Buote (1996) made similar comparisons to ROSAT data. The results of Mohr et al. favor a high density universe, $\Omega = 1$. Buote & Xu (1996) reach the opposite conclusion. We discuss possible sources of this discrepancy in Chapter 4, and by comparison to our simulation identify a small bias in the results of Buote & Xu.

In order to be interpreted these effects should be calibrated using simulations. Unfortunately, the X-ray luminosities of clusters, being proportional to the square of the electron density, are dominated by the dense cluster cores. Accurately simulating these cores requires extremely high resolution and corresponding computational resources. The radiative cooling of the plasma must be included in simulations of

the largest clusters, where cooling flows may increase the central densities. Using simulations to calibrate cluster baryonic mass estimates and measurements of the Sunyaev-Zel'dovich effect also requires resolution of cluster cores.

Extracting cosmological information from cluster structure requires that substructure be quantified. Unfortunately, some measures of substructure in the X-ray images of clusters have also been most sensitive to cluster cores (Mohr et al. 1993, Evrard et al. 1993). However, Buote & Tsai (1995) have proposed a substructure statistic based on the power in multipole moments of the projected gravitational potential. Their so-called "power ratios" are most sensitive to structure outside the cluster cores. With this statistic substructure can be quantified in simulated clusters without the need for ultra-high resolution cores and cooling. Once substructure statistics have been established, we can study substructure survival time, the expected distribution of substructure statistics, and the evolutionary history of clusters measured in the space of the substructure parameters.

Another advantage of the power ratio statistics for quantifying substructure is that they are most sensitive during the earliest stage of the merger, as the subclump falls toward the main cluster. In effect, as viewed via power ratios, the merger ends before the complex dynamical processes of gas relaxing to hydrostatic equilibrium take place in the core. This is advantageous both for simulations, as the modelling of these processes is less important, and for making models to describe the merger events themselves. In Chapter 5 we fashion such a model by combining the merger rate, based on the Press & Schechter (1974) formalism, with a simple model describing the infall of a subclump onto the main cluster.

In order to simulate clusters for study I have developed a new code, combining an adaptive N-body code for evolving collisionless dark matter and a fixed resolution hydrodynamics code for evolving collisional gas. Grid based Eulerian gas codes have been used in engineering and scientific applications for many years and have been well studied (Ryu et al. 1993, Bryan et al. 1995). They are limited, however, by finite computational resources. Accurate cluster simulation requires that the mass field in a large computational volume be computed, and high spatial resolution requires a

prohibitively large computational grid. Lagrangian approaches make more efficient use of computational resources by allowing spatial resolution to flow to where it is most needed. Smooth Particle Hydrodynamics (SPH), for example, uses particles as elements of both mass and force resolution. This technique excels in high density regions but does a poor job in low density regions where particles are few. Moving grid techniques developed recently (Gnedin 1995, Pen 1995) also concentrate computational effort, but can have problems in regions where the flow is highly deformed. Finally, Eulerian techniques which employ adaptively nested levels of resolution are being implemented presently and are very promising as they are, conceptually at least, only marginally more complicated than the single grid methods on which they are based (Bryan 1996). While all these methods are useful, the single fixed grid Eulerian methods are the simplest and best understood. One of these, the Piecewise Parabolic Method (PPM) (Colella & Woodward 1984) as implemented in the KRONOS code (Bryan et al. 1995), is the basis for the hydrodynamic portion of my code, described in Chapter 2.

As described above, the combination of a fixed, high resolution grid and a large spatial volume can be satisfied only at high computational cost. I have therefore borrowed from the Lagrangian philosophy the idea of solving the relevant equations only where the computational effort is most fruitful. Specifically, the accurate simulation of a cluster requires evolving the mass field in a large volume around the cluster because gravity is a long range force. The equations of gasdynamics, however, are short range, and as such need only be solved in a much smaller volume around the cluster. I have therefore developed a code which evolves the mass and gravity fields in a large volume and the gas density, velocity and energy fields in smaller, embedded volume.

The Poisson equation and Euler's equations each require that boundary conditions be prescribed. The usual procedure for cosmological simulations is that periodic boundary conditions be applied. This can still be done for the mass and gravity fields. Since the gas is only explicitly evolved in a subvolume of the total simulation, its boundary conditions must be handled differently. The total mass field is represented by dark matter particles in most of the volume, and by dark matter particles and the

gas density field in the gas subvolume. Therefore the gas is assumed to follow the dark matter outside the gas subvolume. At the edge of the gas subvolume, boundary conditions for the gas can be estimated from the dark matter. Determining the total mass and velocity fields from the particle distribution is straightforward. The gas can be assumed to have identical velocity and density in proportion to the mean gas mass to total mass ratio. The gas evolves adiabatically until shocks form, and since the main shocks in a cluster's formation begin at the cluster center and propagate outward, the gas energy, temperature and pressure at the boundary can be assigned assuming the gas entropy is still primordial.

In chapter 2 we present a description of the simulation code, with additional details given in the appendix. Chapter 3 describes the cosmological model we simulate. Chapter 4 presents statistics for measuring substructure and its survival time and analyzes the simulation in light of those statistics. In Chapter 5 we present a model for determining the dependence of the power ratios on cosmological parameters. Chapter 6 presents conclusions.

Chapter 2

The Code

The simulations were performed using a hybrid code constructed from two well tested codes, the P3M2 code of Bertschinger & Gelb (1991) and the KRONOS code of Bryan et al. (1995). The combined code is called P8M3[1].

The P3M2 code solves the equations of Newtonian gravity and dynamics for a system of collisionless particles in a Friedmann-Robertson-Walker cosmology. Comoving spatial coordinates x are used, and the time coordinate τ (not conformal time) is related to proper time t by $d\tau = dt/a^2$, where a is the expansion factor which relates proper distance (r) to comoving distance (x) by $dr = adx$. In these coordinates, with $a = 1$ corresponding to the present, Poisson's equation becomes

$$\nabla^2\phi = 4\pi G a^2 \bar{\rho}\delta\,, \tag{2.1}$$

where G is Newton's gravitational constant, $\bar{\rho}$ is the mean proper mass density, $\delta = \rho/\bar{\rho} - 1$ is the overdensity, and ϕ is related to the Newtonian gravitational potential Φ by $\phi = \Phi - 2\pi G a^2 \bar{\rho} x^2/3$. The equation of motion for the collisionless dark matter particles is

$$\frac{d^2\vec{x}}{d\tau^2} = a^2\vec{g}\,, \tag{2.2}$$

[1]P3M stands for Particle-Particle–Particle-Mesh and is more properly written P^3M. P3M2 utilizes an extra, adaptive layer of refinement with a finer scale P^3M calculation, hence it is more properly written $(P^3M)^2$. The KRONOS code uses the Piecewise Parabolic Method, or PPM. Combining powers, $(P^3M)^2 \cdot PPM = P^8M^3$.

where $\vec{g} = -\nabla\phi$ is the gravitational acceleration.

The equation of motion for the particles is integrated by the second order accurate leapfrog technique,

$$\begin{aligned} \vec{x}^{n+1/2} &= \vec{x}^{n} + \vec{v}^{n}\Delta t^{n}/2 \\ \vec{v}^{n+1} &= \vec{v}^{n} + \vec{g}^{n+1/2}\Delta t^{n} \\ \vec{x}^{n+1} &= \vec{x}^{n+1/2} + \vec{v}^{n+1}\Delta t^{n}/2\,, \end{aligned} \tag{2.3}$$

where the superscript n is the timestep index.

The Poisson equation is solved approximately in several steps. First, long range forces are calculated by the particle-mesh (PM) technique. In regions of low particle density a short range correction is applied to each pair force in a direct sum over pairs of near neighbors. Together, these two steps are called particle-particle – particle-mesh, or P3M (Hockney & Eastwood 1981). In regions of high particle density, the computational cost of direct pair summation can be prohibitive. Here an adaptive technique is used in which a fine grid is used to perform a second level PM calculation, followed by a further pair summation over only very near neighbors. The short-range (PP) correction to the long-range (PM) force is designed to produce a net pairwise force given by a Plummer law, $\vec{F} = Gm_1m_2(\vec{r}_2 - \vec{r}_1)/[(\vec{r}_2 - \vec{r}_1)^2 + \epsilon^2]^{3/2}$, which weakens at short range to minimize two-body relaxation and to maintain the accuracy of the time integration.

The KRONOS code solves Euler's equations of inviscid, compressible fluid flow, while also solving the Poisson equation and integrating the trajectories of dark matter particles. The KRONOS gravity solver uses the strightforward PM technique, but in the combined code P3M2 performs the gravity calculation and leaves KRONOS to handle the gas dynamics only. The equations governing the gas evolution are

$$\frac{\partial}{\partial t}\rho_b + \frac{\partial}{\partial r^i}\rho_b v^i = 0\,, \tag{2.4}$$

$$\frac{\partial}{\partial t}\rho_b v^j + \frac{\partial}{\partial r^i}(\rho_b v^i v^j + P\delta^{ij}) = \rho_b g^j\,, \tag{2.5}$$

$$\frac{\partial}{\partial t}E + \frac{\partial}{\partial r^i}(E+P)v^i = \rho_b v^j g^j \,, \tag{2.6}$$

where ρ_b is the baryonic (gas) proper density, $\vec{v}$ is the proper velocity, P is the gas pressure, E is the total gas energy density, and $\vec{g}$ is the gravitational acceleration vector. Cosmological flows often occur in which high bulk flow velocities cause the total gas energy to be dominated by the kinetic energy, so that small relative errors in the total energy integration can yield very large temperature errors. In order to accurately integrate the gas temperature (or equivalently the internal energy or pressure) KRONOS also integrates the following equation for the gas internal energy density e:

$$\frac{\partial}{\partial t}e + \frac{\partial}{\partial r^i}ev^i = P\frac{\partial}{\partial r^i}v^i \,. \tag{2.7}$$

Like P3M2 the KRONOS code also uses a comoving coordinate system, but with different time, mass, velocity, energy and gravity variables. The combined P8M3 code calculates conversion factors for these quantities.

The gas equations are integrated numerically by the Piecewise Parabolic Method (PPM), a third order accurate, grid-based technique in which the cell-averaged gas variables (density, velocity and energy) are represented on a grid and the three dimensional fluid equations are solved as a series of one dimensional problems. PPM is one of a general class of higher order Godunov methods which employ a Riemann solver to calculate mass, momentum and energy fluxes through cell faces. PPM can resolve shocks in one or two grid spacings. Good descriptions of the method are given in (Colella & Woodward 1984, Bryan et al. 1995).

Two versions of the combined P8M3 code have been written; one for serial and shared memory parallel machines and another which uses message passing for a distributed memory parallel computer. Some of the technical aspects of these two implementations are different, and will be described below.

Combining the P3M2 and KRONOS codes required changes to the treatment of gravity by the gas code as well as establishing communication between the two algorithms. As originally written, KRONOS used a simple PM gravity solver which produced the gravitational potential on the gas grid. This potential was differenced

wherever the gravitational force was needed. The P3M2 code produces more accurate gravitational forces directly, with no differencing of potential, by using four Fourier transforms ($\rho \rightarrow \hat{\rho}$, $\hat{g}_i \rightarrow g_i$) instead of two ($\rho \rightarrow \hat{\rho}$, $\hat{\phi} \rightarrow \phi$). Therefore instances of potential differencing in the KRONOS portion of the combined P8M3 code were changed to use the P3M2 force directly. The P3M2 gravity solver also utilizes a high order interpolation function, TSC (Triangular Shaped Cloud) (Hockney & Eastwood 1981) and an optimized, anti-aliased Green's function, as opposed to the lower order CIC (Cloud In Cell) (Hockney & Eastwood 1981) interpolant and simple Green's function of KRONOS.

The necessary communication between the gravity and gas portions of the code was implemented differently in the shared and distributed memory versions of the program. The shared memory code adopts the basic structure of KRONOS, with calls to P3M2 routines where necessary. The distributed memory code is based on the P3M2 code, with calls to KRONOS routines. In each, when calculating the density field or gravity, each gas cell is treated as a "particle" with the appropriate mass. This is accomplished in the shared memory code by adding a loop over gas cells wherever there was a loop over dark matter particles in the gravity routines. For example, the original P3M2 code contains a loop over particles in which the mass of each particle is interpolated onto the density grid in preparation for the PM force calculation. The combined code adds a loop over gas cells and treats each of those cells as a "particle" with mass equal to the gas density times the volume of the gas cell.

In the original distributed memory P3M2 code, each processor maintains a list of particles which reside in a particular volume. To account for the gas in the combined code, these particle lists are expanded to include gas "particles." Hence the gas has two representations, one as a grid of density, velocity and energy, and another as "particles" with mass and velocity. The former representation is used by KRONOS, the latter by P3M2. These two representations must, of course, be kept consistent. For this purpose special routines were written to send portions of the gas grid, which is maintained on a single processor, to the processors whose assigned spatial volumes

overlap the gas volume. These processors then use the gas density and velocity to update the masses and velocities of the gas "particles" contained in their particle lists. This procedure is shown schematically in Figure A.2. On the left is a representation of a 5^3 grid of gas data (e.g., density), which resides physically on processor 0. On the right is a particle list (e.g., mass) which resides physically on, say, processor 5. The two shaded slabs of the gas grid in this example lie within the portion of the simulation volume assigned to processor 5. Hence, for each of these shaded gas cells the processor 5 mass list has an entry. A separate list of particle indices stores a global integer tag for each particle, for which there is a one to one correspondence between the tag of a gas "particle" and it's location in the gas grid. A similar procedure is used to send the calculated gravity at each gas "particle" back to the gas grid.

The basic code structure for the distributed memory version of the code is represented in Figure A.2. This shows that at the beginning of each timestep, gas density and velocity are sent from the gas grid to the particle lists. The gas density is used in the construction of the total density field needed for the PM force calculation. The leapfrog integration scheme (Eqn. 2.3) for the dark matter trajectories and the Riemann solver used by KRONOS require the density field to be evaluated one half timestep ahead of the current time. For the dark matter particles this is easily accomplished by integrating their positions forward one half step before performing the force calculation. To approximate the gas density at one half timestep ahead, the particle representation of the gas is used, and the gas "particles" are moved off their fixed grid postions by $\vec{v}\Delta t/2$. This is why the gas velocity must be passed from the gas grid to the particle lists before the computation of the total density field begins. Note however, that the gas "particles" must be returned to their grid positions after the total density is computed so that the gravitational force felt by each gas "particle" is the force at the grid position at the center of the gas cell.

The gas solver (KRONOS) requires boundary conditions for the gas volume at the beginning of the timestep. As these are determined from the dark matter density and velocity fields, they must be computed before the particle positions are integrated forward the first half timestep. For this calculation, each processor determines which

portion of the gas volume, if any, resides locally, and then uses TSC interpolation to compute the density and momentum density fields at the boundary cells of the gas volume. Dividing the latter by the former gives the velocity field at these points. The density and velocity boundary values are then passed from the particle list structure on each processor to the gas grid structure on processor 0.

Next, the particle postions are integrated forward one half timestep and the gravity calculation commences, modified only[2] to move the gas "particles" back to their grid positions after the total density is calculated, as described above. Then the particle velocities are updated by one full timestep and the positions by the second half timestep.

After the gravity calculation, the gravitational acceleration at each gas "particle" must be passed back to a grid structure on processor 0. KRONOS is called next, to update the gas variables by a full timestep, and the next timestep can begin.

[2]Other modifications to the gravity code were added to minimize memory usage. These, however, are independent of the changes made to combine the gas and gravity codes.

Chapter 3

The Model

We evolve a cosmological model which is consistent with observational constraints (Ostriker & Steinhardt 1995, Liddle 1996, Kochanek 1996).

$$H_0 = 100h \text{ km s}^{-1}\text{Mpc}^{-1} = 75 \text{ km s}^{-1}\text{Mpc}^{-1} \tag{3.1}$$

$$\Omega_{CDM} + \Omega_B + \Omega_\Lambda = 1 \tag{3.2}$$

$$\Omega_B = 0.015h^{-2} = 0.0267 \tag{3.3}$$

$$\Omega_{CDM} + \Omega_B = 0.3\,. \tag{3.4}$$

Within this cosmological context we simulate a 51.2 Mpc comoving volume with the dark matter density field sampled using 6069442 particles with nested mass resolution. The innermost 16 Mpc cube contains particles with a mean spacing of 100 kpc (comoving), corresponding to a mass of $4.7 \times 10^7 M_\odot$ per particle. This is the total mass of a 100 kpc cube at mean density, including dark matter and baryons (gas). When dark matter particles fall into the gas-filled volume their mass is scaled down by $\Omega_{CDM}/(\Omega_{CDM} + \Omega_B)$. A layer 4 Mpc thick holds particles with twice the spacing and eight times the mass of the central cube. Two more layers of 6.4 Mpc and 7.2 Mpc each have a further coarsening of the mass resolution by the same factors over their inner neighbor. The largest particles then have masses of $2.4 \times 10^{10} M_\odot$ and reside at least 18.4 Mpc from the center of the simulation volume. These distant,

massive particles provide the tidal forces under which the cluster will evolve.

The central 10 Mpc (comoving) volume also contains a grid of 100^3 gas cells. The mean gas mass per cell is $4.2 \times 10^6 M_\odot$.

Initial conditions are generated using the COSMICS package of Bertschinger (1995) First, the linearized Einstein and Boltzmann equations are integrated to compute the matter transfer function. An initial Harrison-Zel'dovich spectrum $P(k) \propto k$ is assumed. The resulting transfer function is used to generated a constrained random realization of initial conditions. The constraint applied is that the central overdensity, when smoothed under a Gaussian of width 6.4 Mpc, would have a value of 0.7, or 2.5σ, where σ is the root mean square value of the smoothed overdensity. The 6.4 Mpc Gaussian encloses the same mass as a 10 Mpc top hat, or $2.0 \times 10^{14} M_\odot$, which is a medium sized cluster. Other simulators (Frenk et al. in progress) have used constrained initial conditions to generate unreasonably large clusters, with the result that the cluster evolution was affected when the nonlinear scale approached the size of the simulation volume. Here we have been careful to chose a perturbation which will result in a good size cluster while ensuring that such a cluster is not an extremely rare event in a volume of this size. Using the fitting formula for peak number density given by Bardeen et al. (1986), we find that the expected number density of 2.5σ peaks in our simulation volume is 0.5.

COSMICS produces a realization of the density and velocity fields (and equivalently, the displacement field) of the mass. The central 100 Mpc volumes in these fields are used to generate the initial conditions for the gas. The gas density is set proportional to the total density, the gas velocity is set equal to the particle velocity. The P8M3 code determines the appropriate temperature field by assuming the gas entropy is constant in space. The mean gas temperature is chosen appropriate to the initial simulation redshift.

Initial particle displacements are determined from the linear transfer function by the Zel'dovich approximation. The initial simulation redshift is set by requiring that the maximum displacement be no larger than 100 kpc, the mean interparticle spacing in the high resolution central volume of the simulation. This results in an initial

redshift of $z_i = 83$.

The gravitational force between particle pairs is softened to a Plummer law, for which the potential energy is given as

$$U = -\frac{Gm_1m_2}{\sqrt{r^2 + \epsilon^2}}, \tag{3.5}$$

with $\epsilon = 0.04$ Mpc. With this softening, the force between a pair of particles 100 kpc apart is 80% of the true (unsoftened) force. In this way the force resolution of the gravity and gas portions of the code are kept consistent at 100 kpc.

Chapter 4

Substructure

Galaxy clusters were first identified optically as regions of high galaxy density projected on the sky. Abell (1958), for example, identified clusters by the number of galaxies projected within a $1.5h^{-1}$ Mpc radius circle. The most obvious property of optical clusters is their richness, which is roughly the number of galaxies. But they also display different morphologies. Abell (1965, 1975) classified his clusters on a sequence from regular to irregular. Zwicky et al. (1961-1968) based their classifications on the relative compactness of the cluster. Bautz & Morgan (1970) devised a classification scheme based on the brightest galaxies in the cluster. Rood & Sastry (1971) developed a system reminiscent of Hubble's "tuning fork" diagram of galaxy types. Morgan (1961) and Oemler (1974) classified clusters by their spiral and elliptical fractions. These classification systems are highly correlated, indicating that cluster optical morphology can be approximately described by a simple sequence from more to less regular (Sarazin 1988). The "ideal" regular cluster would have spherically symmetric distribution in position, and the line-of-sight velocity distribution would be Gaussian, although the velocity dispersion generally decreases with radius from the cluster center (Sarazin 1988).

Irregularity in clusters sometimes manifests itself as multiple peaks in galaxy number density, either projected or in redshift space, indicating that a merger has recently occurred. Geller & Beers (1982) found that 40% of rich clusters have multiple projected density maxima. Dressler & Shectman (1988) made use of velocity information

also and claimed to find significant substructure in 30-40% of clusters. West & Bothun (1990) find "definite substructure" on Mpc scales in 30% of their sample.

Clusters can be imaged with better statistics in X-rays, as there are many more X-ray photons than galaxies available. Forman & Jones (1970) and Jones & Forman (1992) developed a classification system based on structure in the X-ray images. Applying this to images obtained by the Einstein satellite, they identified about 20% of their clusters as "double" or "complex." Mohr et al. (1993, 1995) proposed statistics for quantifying substructure in X-ray images and applied them to Einstein data. By comparing these to simulated clusters (Evrard et al. 1993) these authors conclude that the observations favor a high value for Ω.

An alternative to observational (optical and X-ray) identification and classification of clusters is the theoretical definition based on mass. Clusters correspond to the highest density regions of an appropriately averaged mass density field. The mass density of the Universe varies on all scales. In order to isolate the scales relevant to clusters, one first smooths the density field on cluster scales. Define the mass density field $\rho(\vec{x})$ and the overdensity

$$\delta(\vec{x}) = \frac{\rho(\vec{x}) - \bar{\rho}}{\bar{\rho}}, \tag{4.1}$$

where $\bar{\rho}$ is the mean density. The density smoothed on mass scale M is then

$$\delta(\vec{x}, M) = \int_0^\infty \delta(\vec{x}')W(|\vec{x} - \vec{x}'|, M)dx', \tag{4.2}$$

where the smoothing window function is spherically symmetric about $\vec{x}$ and has compact support. The mass scale M is related to a length scale R_s by

$$M = \int_0^\infty \bar{\rho}W(r, M)4\pi r^2 dr. \tag{4.3}$$

Clusters are then identified with the regions above some threshhold in the smoothed density field. If this field corresponds to the present, then this threshhold density will be around 200 (Lacey & Cole 1993). Because the effects of non-linear gravitational

evolution dictate the spectrum of density fluctuations at present, it is more convenient to work with the initial, linear density field. The statistics of this field are dictated by the cosmological model, and are specified by a power spectrum of density fluctuations which are usually assumed to be Gaussian. The high density regions in this smoothed initial density field are assumed to evolve into galaxy clusters.

This cluster definition, based on the firm mathematical grounds of density fields, power spectra, smoothing functions, etc., is attractive to theorists but not easy to connect to observations. It is most useful for predicting things like the mass distribution of clusters as a function of time, something which is not easy to observe.

In practice there are two approaches for studying cluster distributions based on the initial density field. In the peaks method (Bardeen et al. 1986), high peaks in the smoothed initial density field are considered to be the locations of non-linear structures in the evolved field. E.g., the highest 10% of the peaks in a density field smoothed on cluster mass scales correspond to the most massive 10% of clusters. Statistics such as the correlation functions of the peaks are then thought to apply to the corresponding clusters as well. The other approach, pioneered by Gunn & Gott (1972) and Press & Schechter (1974) and extended by Bond et al. (1991) and others, utilizes the analytic solution for the collapse of a spherical overdensity. The power spectrum of fluctuations in the smoothed initial density field determines the distribution of overdense regions. Each of these regions is modelled as a spherical perturbation in an otherwise flat Universe to give both a mass and a collapse time for that mass. This prescription has been used to determine tha mass function of non-linear structures as a function of time (Press & Schecter 1974), as well as the merger rates, formation histories, and survival times of dark matter halos (Lacey & Cole 1993, Kauffmann & White 1993).

This thesis deals with a simulated X-ray cluster and with statistics based on the initial density field. Because the simulation resolution and input physics are not sufficient for modelling individual galaxies within the cluster, galaxy counts or cluster richness are not useful criteria for defining or classifying clusters or for measuring substructure. Instead we opt for the following definition: a cluster is a spatially

isolated high density region which contains hot, diffuse X-ray emitting gas, and which formed from the mass in a high density region of the initial density field.

In order to make a clear definition of substructure within clusters it is useful to define what substructure is not. A substructureless cluster is spherically symmetric. Departures from symmetry, then, are indications of substructure. However, we wish to avoid any definition of substructure which divides clusters into substructure "haves" and "have nots," since there is of course continuum of degrees of departure from symmetry. Such a division would be artificial. A better approach is to allow operational definitions of substructure based on quantifiable measures. This way we avoid terms like "significant substructure."

4.1 Substructure Statistics

One attempt at quantifying substructure in X-ray maps of clusters of galaxies is due to Mohr et al. (1993). They develop statistics based on the Fourier transforms of annuli in a circular image aperture. Each annulus of some specified thickness and mean radius $\bar{r}$ can be decomposed in a Fourier transform

$$I(\theta, \bar{r}) = \sum_{m=0}^{\infty} A_m(\bar{r}) \cos(m\theta) + B_m(\bar{r}) \sin(m\theta) \,. \tag{4.4}$$

The coefficients A_n and B_n are then

$$A_n = \frac{1}{\pi} \int_0^{2\pi} I(\theta, \bar{r}) \cos(n\theta) d\theta \,, \tag{4.5}$$

$$B_n = \frac{1}{\pi} \int_0^{2\pi} I(\theta, \bar{r}) \sin(n\theta) d\theta \,. \tag{4.6}$$

The center of each annulus is not determined *a priori*, but is instead set to be the position for which the difference between the center and centroid of the annulus is minimized. Specifically, this corresponds to minimizing $A_1^2 + B_1^2$.

For each annulus, a centroid shift is calculated. The emission weighted centroid

shift is

$$w_x^2 = \frac{\sum_j N_j(\vec{x}_j - \langle\vec{x}\rangle)^2}{\sum_j N_j}\,, \tag{4.7}$$

where j is the annulus index, $\vec{x}_j$ is the annulus centroid position, N_j is the photon count in the annulus, and $\langle\vec{x}\rangle = \sum N_j\vec{x}_j/\sum N_j$ is the emission weighted mean centroid.

Mohr et al. (1993, 1995) also introduce an axial ratio

$$\eta(\bar{r}) \simeq 1 - \frac{2\sqrt{A_2^2 + B_2^2}}{r(dI/dr)} \tag{4.8}$$

and an ellipsoidal orientation angle

$$\theta(\bar{r}) = \frac{1}{2}\tan^{-1}(\frac{B_2}{A_2})\,, \tag{4.9}$$

as well as averages and variances (over annuli) of each of these. [1]

In Evrard et al. (1993) these authors apply these statistics to clusters simulated under different cosmological models and argue that the statistics discriminate well between models of different density, though not between low density models ($\Omega = 0.2$) with and without a cosmological constant providing spatial flatness. Mohr et al. (1995) apply these statistics to a sample of Einstein clusters and find that the distributions of centroid shift and axial ratio agree better with their $\Omega = 1$ CDM simulations than with their low density simulations.

Another method for quantifying X-ray substructure was proposed recently by Buote & Tsai (1995). Their power ratio statistics are based on the multipole expansion of two dimensional gravitational potential, which solves the two dimensional Poisson equation sourced by the projected mass density Σ interior to an aperture radius R,

$$\nabla^2\Psi = 2\pi G\Sigma\,. \tag{4.10}$$

[1] Equation 2.8 of Mohr et al. (1995) is incorrect and should be $\theta_0 = \sum_j N_j\theta_j(\bar{r})/\sum_j N_j$.

The multipole expansion is given by

$$\Psi(R,\phi) = -2Ga_0 \ln(1/R) - 2G \sum_{m=1}^{\infty} \frac{1}{mR^m}(a_m \cos m\phi + b_m \sin m\phi)\,, \tag{4.11}$$

$$a_m(R) = \int_{r\leq R} \Sigma(r,\phi) r^m \cos m\phi \;\; r dr d\phi\,, \tag{4.12}$$

$$b_m(R) = \int_{r\leq R} \Sigma(r,\phi) r^m \sin m\phi \;\; r dr d\phi\,. \tag{4.13}$$

The power in the mth multipole due to mass interior to R is the azimuthally averaged value of the square of the mth term in equation 4.11,

$$P_m(R) = \frac{1}{2\pi}\int_0^{2\pi} \Psi_m(R,\phi)\Psi_m(R,\phi) d\phi\,, \tag{4.14}$$

which reduces to

$$P_0 = [2Ga_0 \ln(R)]^2\,, \quad P_{m>0} = \frac{4G^2}{2m^2R^{2m}}(a_m^2 + b_m^2)\,. \tag{4.15}$$

The projected mass density Σ, while available in principle from weak lensing maps of clusters, is not in practice well determined for any real clusters. Buote & Tsai (1995, 1996) were concerned with the dynamical state of clusters and argued that while this would be best reflected by using the projected mass density Σ, the X-ray surface brightness would be an adequate mass tracer. In fact, since the X-ray surface brightness is proportional to the projection of the square of the gas density, the substructure in X-rays will provide a stronger signal than that in projected mass.

One can see immediately the advantage of this statistic over those of Mohr et al. (1993) when quantifying substructure in simulations. The power coefficients a_m and b_m differ from the moment coefficients A_m and B_m in their integrands by a factor of r^m, making the power ratios sensitive to structure on the scale of the viewing aperture instead of structure in the simulated cluster core, where cooling physics is important and uncertain and the spatial resolution is insufficient.

Which of these statistics is "best" for studying clusters depends strongly on the

scale on which the cluster structure is being investigated. Compared to the centroid shift and axial ratio statistics, power ratios are more sensitive far from the cluster center, and different scales can be selected for study by adjusting the image aperture radius. However, the power ratios are more reliably calibrated against simulations, due to the fact that the cluster core is simulated less accurately than the outer cluster due to finite force resolution and the complications of modelling the cooling and contraction of the gas.

Another advantage of the power ratio statistics is that they are relatively noise free compared to the Mohr et al. (1993) statistics. Figure A-3 shows the emission weighted centroid shift (Eq. 4.7) plotted versus expansion factor. Because a small change in the X-ray image can cause the centers of all the annuli to shift, the centroid shift jumps around from timestep to timestep in the simulation. Compare this to Figure A-9, which shows the power ratios varying smoothly with time. Also note that the difference between the largest centroid shifts and the mean value is a factor of only a few. Comparing Figure A-3 to Figure A-9 shows that the primary merger events show up as peaks in both figures, but that the maximum power ratios are more than 10 times the mean values, making them easier to detect unambiguously. For these reasons we concentrate on the power ratios in our analysis.

4.2 Cluster evolution in power ratio space

Figures A-4, A-5 and A-6 show the path of the cluster in the space of the P_2/P_0 and P_4/P_0 power ratios from $z = 10$ to $z = 1$ for the $x - y$, $y - z$, and $z - x$ projections, respectively. In these plots and the following discussion we take the decimal log of the above defined power ratios and refer to these as power ratios, with the logarithm implied. The high density of points near the center of each of these figures indicates that the cluster spends most of its life near the center of its "territory" in power ratio space. Figure A-7 combines the three projections and shows clearly that this cluster spends most of its life with power ratios $-7 \leq P_2/P_0 \leq -6$ and $-10 \leq P_4/P_0 \leq -8$. However the allowed region in the $P_2/P_0 - P_4/P_0$ plane is much larger, extending

approximately from $(P_2/P_0, P_4/P_0) = (-8.5, -11.5)$ to $(P_2/P_0, P_4/P_0) = (-4, -5)$. Between these extremes the allowed region of the plane is a thick filament.

This region of the $P_2/P_0 - P_4/P_0$ plane was identified by Buote & Tsai (1996), who interpreted it as an "evolutionary track." They were able to confirm this interpretation using 6 simulated clusters, with simulated X-ray images available at only a few redshifts. These plots, showing a nearly continuous path in this power ratio plane, offer spectacular confirmation of their observation.

Closer inspection of these figures reveals that the trajectory of the cluster in this power ratio plane consists of periods in the central part of the allowed region interrupted by excursions out from the center, usually up to the high power region, then down to the low power region, and then gradually back to the center. The excursions to the high power region of the plane generally are direct, progressing up in P_2/P_0 and in P_4/P_0 simultaneously. Excursions to lower power sometimes occur in only one coordinate direction, but usually in both.

Physically, what is occurring to the cluster to cause these excursions? In agreement with the interpretation of Buote & Tsai (1996), we find that excursions to high power occur during a merger event. As a subclump of X-ray gas first begins to cross within the 1 Mpc aperture radius for which these power ratios were computed, both the P_2/P_0 and P_4/P_0 ratios begin to increase. In each case, the P_4/P_0 ratio peaks just before the P_2/P_0 ratio, and the peak in P_2/P_0 is wider (in time) than the peak in P_4/P_0. This can be seen in Figure A-8, in which P_2/P_0 and P_4/P_0 are plotted against expansion factor $a = 1/(1+z)$ for a representative high power excursion. In the plots of P_4/P_0 versus P_2/P_0 this fact is revealed in the clockwise direction in which the cluster trajectory moves up, around and down in its high power excursions in power ratio space.

For most of the high power excursions the return path in $P_2/P_0 - P_4/P_0$ space is a concave path whose shape can be understood in terms of a simple model. Consider the case of a point source with luminosity Σ_1 falling on to a much brighter pointer source with luminosity Σ_0. Most of this cluster's mergers consist of single small clumps falling into the main cluster, so consideration of each as a point source can

reveal the qualitative behavior. For this argument we ignore the slight shift in the center of the aperture caused by minimizing P_1. When the small source crosses into the aperture (radius R) surrounding the main source, the powers are given by

$$P_2 = \frac{1}{8}\Sigma_1^2\left(\frac{r}{R}\right)^4, \tag{4.16}$$

$$P_4 = \frac{1}{32}\Sigma_1^2\left(\frac{r}{R}\right)^8 \propto P_2^2. \tag{4.17}$$

P_0 is the same for each, so in the $P_2/P_0 - P_4/P_0$ plane this trajectory is a parabola. Actual trajectories are more complicated, but qualitatively similar.

Excursions to low power regions of the $P_2/P_0 - P_4/P_0$ plane take a variety of paths. Many of these consists of a general decrease, then increase, in both P_2/P_0 and P_4/P_0 simultaneously. However, there are also excursions which occur parallel to one power ratio axis or the other. In other words, P_2/P_0 decreases, then increases, while P_4/P_0 remains almost constant. Or P_4/P_0 cycles down and up while P_2/P_0 stays fixed. Excursions at fixed P_2/P_0 to low P_4/P_0 correspond to the higher order components of the X-ray structure of the gas relaxing away, while the $m = 2$ mode is being preserved by the linear nature of a dominant filament which stretches across the aperture. The P_4/P_0 ratio measures "boxiness," while the P_2/P_0 ratio measures the linearity of the cluster substructure. Excursions to low P_2/P_0 at fixed P_4/P_0 occur when the linear nature of the substructure becomes less pronounced relative to the "boxiness."

These types of behavior are indicated by Figures A-9, A-10 and A-11, which show the power ratios plotted versus expansion factor. For an example, study Figures A-9 and A-10, which depict the trajectories in the power ratio plane for the $x - y$ and $y - z$ projections. At an expansion factor just greater than 0.2, P_2/P_0 reaches a local minimum while P_4/P_0 is at a local maximum. This corresponds to the horizontal low power excursion in Figures A-4 and A-5. This feature is most prominent in the $x - y$ projection, but the actual sequence of mergers which produce this part of the trajectory is most clearly seen in the $y - z$ projection of the X-ray surface brightness. This is depicted in Figure A-12, which shows the X-ray surface brightness at a few

key times in this merger sequence.

Panel A shows the cluster as an X-ray bright clump falls in from above. Both P_2/P_0 and P_4/P_0 are large. Panel B depicts the situation 15 simulation timesteps later. The isophote contours in each panel are separated by one decade each, with the highest contour at 10% of the maximum X-ray surface brightness. Because the central luminosity of the cluster has increased, the subclump falling in from above now appears as an elongation of the isophotes. Another, albeit smaller, subclump is falling in from below the cluster center. These two subclumps are not falling exactly radially onto the cluster center. Instead, they will collide just left of the cluster center, as shown in panels C and D. At panel C, P_2/P_0 reaches a minimum, then abruptly begins increasing. By panel D linear structure is obvious again, although now it is aligned perpendicular to the filament along which the two subclumps entered the cluster. P_4/P_0 has remained relatively constant, at a maximum, as the "boxy" structure remains, here as a combination of the left-right orientation of the main cluster and the up-down orientation of the main filament. In panel E the left-right alignment cluster is still apparent, and is reflected in the large value of P_2/P_0. Panel F shows the left-right structure relaxing away, while a new subclump approaches the cluster from below. P_2/P_0 is still decreasing, but the combination of the remaining left-right structure in the highest isophotes and the up-down structure imposed by the bottom subclump results in an increasing P_4/P_0. By panel G, the dominant structure is again the up-down alignment resulting from the merger of the bottom subclump.

The whole history of cluster mergers of this sort is contained in figures A-13, A-14 and A-15, which show the time evolution of the P_2/P_0 and P_4/P_0 power ratios. Apparent in these figures is the "bouncing ball" nature of the trajectories, with more or less rounded peaks separated by "bounces" in which the declining trajectory abruptly reverses itself and begins to rise again to a new peak. This behavior is the norm early in the cluster's history, becoming less frequent as it evolves. The reason for these "bounces" is that mergers are occurring frequently at these early times. After the power ratios peak and begin to decline, but before they can relax to an equilibrium value, a new merger begins as another clump of hot gas falls into the power ratio aper-

ture. The frequency of these high power events decreases with time, as the ever more massive cluster will only show high power ratios when mergers with more massive subclumps occur.

Also evident in figures A-13, A-14 and A-15 is the fact that while the power ratios vary greatly on the timescale of individual merger events, they do not vary greatly on much longer timescales. This can also be seen in figure A-16, in which the amount of time spent at points in power ratio space is shown as a contour plot. The contours are made by overlaying the trajectories in power ratio space for the three projections of the P_2/P_0 - P_4/P_0, which are shown individually in figures A-4, A-5 and A-6. The points along the trajectories are binned in the P_2/P_0 - P_4/P_0 plane then smoothed with a Gaussian. Superimposed on these contours are points corresponding to the power ratios measured by Buote & Tsai for their sample of clusters observed by ROSAT. Of course, the ROSAT clusters are at lower redshift than the simulated cluster. But even over the huge redshift range from $z = 10$ to $z = 1$, the cluster occupies the same region of power ratio space as the ROSAT clusters. In addition, the single simulated cluster corresponds to a single perturbation scale, while the data are drawn from clusters with a range of perturbation scales. Still, the shape of the distributions for the simulation and the real data are very similar.

4.3 Substructure survival time

Richstone et al. (1992) and others have argued that the fraction of observed clusters possessing substructure reflects the cosmic mean matter density. In a low density universe, matter approaches free expansion at late times. Consequently, observed structures must have formed early, when the mean density was closer to critical. Clusters formed at early times would have had time to relax and would appear today with little substructure. In order to quantify this effect one requires knowledge of the cluster formation or merger rate as well as the relaxation time scale of the substructure which results from these mergers.

Using the solution for the collapse of an overdense homogeneous spherical per-

turbation in a Friedman-Robertson-Walker universe and assuming a Gaussian distribution for the density on cluster scales, Richstone et al. compute the fraction of clusters which collapse within a certain time interval of the present epoch. If this time interval is chosen to be the amount of time for which evidence of recent merger activity survives, then this fraction of clusters "recently formed" will be the same as the fraction of clusters which show evidence of current or recent mergers. In brief, their argument is as follows.

A homogeneous spherical overdensity above the critical density will collapse at a time which is a monotonic function of the overdensity. A distribution of overdensities then leads directly to a distribution of collapse times as a function of the initial overdensity. The chosen initial density distribution is Gaussian, and its variance is chosen so that the derived fraction of the mass on the scale of $10^{15}M_{\odot}$ which has already collapsed is equal to the mass fraction of the universe in Abell clusters with masses of about $10^{15}M_{\odot}$. Finally, they derive an expression for the fraction of existing clusters which have collapsed within the last time interval δt.

Applying this expression requires determining the fraction of clusters which show recent merger activity and choosing a value for δt, which should be the amount of time for which merger activity remains visible in clusters. Interpreting cluster substructure as evidence of recent merger activity, Richstone et al. argue, based mostly on optical studies, that 25% of rich clusters show substructure at present. These authors have concentrated on predicting cluster formation and merger rates and have made simple assumptions about the relaxation time scale of substructure based on the cluster dynamical time or crossing time. They assume that low contrast substructure is erased in about $0.1/H_0$. Their results favor $\Omega \geq 0.5$.

Lacey & Cole (1993) perform a similar calculation. They equate the fraction of rich clusters with significant substructure to the fraction of clusters which "formed" within some specified time interval of the present. They define the cluster formation time as that time at which the halo mass first increased to 50% of its present value. They find that matching observations with a CDM spectrum requires $\Omega \geq 0.6$ if they assume that substructure is erased on a timescale of 20% of the present age of the

Universe.

Kauffmann & White (1993) apply the formalism of Press & Schechter (1974) to study the merger history of dark matter halos. They argue that uncertainty in substructure survival time precludes using their results to predict Ω from cluster substructure.

Richstone et al. (1992) and Lacey & Cole (1993) both characterized observations of substructure with a single number: the fraction of clusters displaying significant substructure. As discussed in the introduction to this chapter, different observers using different selection criteria have arrived at different values for this fraction, ranging from 20% to 40%. This much variation seems inevitable when there is no consensual definition of substructure. We avoid this dilemma by relying on a set of quantitative statistics, the power ratios, to place each cluster on the continuum of cluster morphologies. Then, rather than relying on subjective determinations of the significance of substructure, we simply assign each cluster a set of power ratios. When the simplicity of a single number is desired or required, we can, for example, consider all clusters with P_2/P_0 above some threshhold value.

Richstone et al. (1992) and Lacey & Cole (1993) also rely on simple estimates of the time interval during which recent merger activity remains visible as substructure. But these estimates are not rigorous, nor are they well motivated by the details of the substructure measurements.

In this section we study the survival time of the substructure, measured as the duration of high power excursions, in our simulated cluster. In chapter 5 we relate these observations to a simple model for the merging events which produce high power ratios.

Figures A-13, A-14 and A-15 show the time evolution of the P_2/P_0 and P_4/P_0 power ratios. If substructure survival time is governed by the physics of gas shocking, cooling, and relaxing into hydrostatic equilibrium, then it should be relatively insensitive to cosmology. If, on the other hand, substructure survival time depends on the merger rates of clusters, then the survival time should depend on the cosmology. As evidenced by these figures, a peak in P_2/P_0 is usually coincident with a peak

in P_4/P_0 and corresponds to the infall of a clump of hot gas onto the main cluster. The survival time of substructure measured this way is just the width of the peak. Clearly, peak width is relatively constant over the entire range of redshift covered. Meanwhile, the cluster mass evolves significantly, increasing by more than a factor of six between $z = 4$ and $z = 1$. Thus, the substructure survival time, as measured by the power ratios, is insensitive to the cluster mass.

Specifically, we define substructure survival time, as related to power ratios, by the full width at half maximum for single peaks in the function $P_2/P_0(t)$, plotted in figures A-13, A-14 and A-15. As the vertical scale is logarithmic, a factor of one half corresponds in the figures to a decrement of $\log_{10} 2 = 0.3$ from the peak. Low peaks which do not fall to one half of their peak value before rising again are not considered single peaks. By this definition, substructure survival time ranges from 0.13 to 0.30 billion years, or about 0.01 to 0.02 H_0^{-1}. Clearly this is much less than the estimate (0.1 H_0^{-1}) of Richstone et al. (1992), who state that their estimate of Ω varies approximately linearly with the substructure relaxation rate. Nakamura et al. (1995) provide the following fit to equation 17 of Richstone et al.

$$\Omega_m \geq \frac{0.26\delta\tilde{F}}{H_0\delta t}, \tag{4.18}$$

with $\delta\tilde{F}$ representing the fraction of clusters which have formed within the last δt. The implication seems to be that this rate of relaxation indicates a value of Ω greater than about 2.5. However, their estimate of Ω results from combining an estimate of substructure survival time with measurements of the frequency of occurrence of substructure classified in a certain way, such as the Jones & Forman (1992) morphological classes. A more fair comparison requires using the power ratios to quantify both the frequency of the substructure and its survival time. Evrard et al. (1993) and Buote & Xu (1996) have tried determining substructure frequency in different cosmological models by simulating many clusters in each model. In chapter 5 we develop an analytic model for substructure frequency and survival time that can be used to rapidly test most cosmological models.

Ideally, a large number of hydrodynamically simulated clusters could be used to quantify exactly the expected distribution in power ratio space for a given cosmological model and as a function of time. Currently that goal is beyond the capabilities of current simulations. However, by using simpler simulations and models for the physics not explicitly simulated, greater numbers of clusters can be generated. Tsai & Buote (1996) used 6 hydrodynamically simulated clusters from an $\Omega = 1$ CDM model universe, and found too many high power clusters compared to ROSAT data, indicating $\Omega < 1$. In order to get better statistics, Buote & Xu (1996) drew clusters from gasless N-body simulations of different cosmologies. To generate simulated X-ray images they assumed $\rho_{\rm gas} \propto \rho_{\rm DM}$ and constant temperature. They found that low Ω CDM models produce power ratios in good agreement with observations, while $\Omega = 1$ "standard" CDM does not.

While we cannot directly check these results, we can test some of the assumptions that underlie them. Figure A-17 shows the cluster trajectory in power ratio space computed once from the X-ray surface brightness and once again from the square of the gas density. This is equivalent to assuming isothermality. Clearly, the trajectories are very similar, with the isothermal assumption leading to overestimates of the power ratios except at the highest power. This overestimate is due to the fact that the cluster gas temperature is not isothermal; rather, it declines with radius. Figure A-18 shows the spherically averaged gas temperature as a function of radius from the cluster density peak. A similar overestimate is seen for the P_3/P_0 power ratio. By neglecting this effect, Buote & Xu (1996) would have overestimated the amount of substructure for a given mean density present in their simulations, and hence would have been led to underestimate Ω. They argue, however, that the measured X-ray surface brightness is actually the emissivity convolved with the ROSAT detector response function, which varies little over the range of cluster gas temperatures. So the degree to which the isothermal assumption leads to an understimate of Ω remains uncertain.

A more significant difference appears when comparing power ratios computed from the X-ray surface brightness and from the square of the dark matter density. Figure A-19 shows the P_2/P_0 power ratios plotted versus expansion factor and computed

from the X-rays, the square of the gas density, and the square of the dark matter density. On average, approximating the X-ray surface brightness as the square of the dark matter density produces significant overestimate of the power ratios. Combining all 3 orthogonal projections of the cluster, we find the mean and root mean square overestimates (in the decimal log of the power ratio) to be 9.3% and 10.5%, respectively. Doing the same for the P_3/P_0 power ratios yields mean and root mean square overestimates of 9.3% and 9.9%. P_4/P_0 overestimates are 10.8% and 11.0%.

Naively correcting for this overestimate in the results of Buote & Xu (1996) means decreasing their value for the mean power ratios for their simulations by 10%. This correction brings their values for the mean power ratios P_2/P_0 and P_3/P_0 for the standard CDM model into good agreement with the values computed by Buote & Tsai (1996) for their sample of ROSAT clusters. At the same time, this correction destroys the agreement seen by Buote & Xu between the data and their simulations of an $\Omega = 0.35$ open CDM model. This reversal of the result of Buote & Xu agrees with the conclusions of Mohr et al. (1995), that the substructure in X-ray clusters is more consistent with a high density than a low density cosmology.

However, this naive correction ignores a point made first by Buote & Tsai (1995), that spatial temperature variations, which are present in the simulated data, are not detected by ROSAT even when present in real clusters. These temperature fluctuations arise due to adiabatic heating in collapsing gas subclumps, and due to shock heating which results when a subclump collides with the main cluster or any of the shock fronts present in the cluster. However, the spectral response of the ROSAT PSPC (Position Sensitive Proportional Counter) is nearly independent of the gas temperature (Buote & Tsai 1995, Pfeffermann et al. 1987).

Recalculating the power ratios for our simulation based on the square of the gas density, as opposed to the X-ray emissivity $\rho^2 T^{1/2}$, results in power ratios closer to those calculated from the square of the dark matter density. The result is still an overestimate; i.e., power ratios computed from the square of the dark matter density are higher than those for the square of the gas density. For P_2/P_0, the mean and root mean square overestimates are 3% and 13% respectively. For P_3/P_0 these numbers

are 4% and 13%, and for P_4/P_0 they are 7% and 12%.

These overestimates, while smaller, are statistically significant. Applying the F-test (Press et al. 1992) to check for significantly different variances in the power ratio distributions reveals consistent variances for the P_2/P_0 and P_3/P_0 ratios, but inconsistent variances in the P_4/P_0 distributions at a significance level of 2.75σ. We use Student's t-test to determine the significance of different means in two distributions. Applying the version of this statistic appropriate for paired statistics we find that the means of the P_2/P_0 and P_3/P_0 ratios differ at significance levels of 3.7σ and 4.0σ, respectively. To compare means of the P_4/P_0 distributions we apply the version of Student's t appropriate for distributions with different variances, and find a 4.6σ significance to the difference in means.

What accounts for this overestimate? There are two reasons why the gas in a cluster will not be distributed exactly as the dark matter. One is that the gas shocks, while the dark matter is collisionless. These shocks create hot spots in the gas which affect the X-ray surface brightness of the cluster but are not expected to appear in the ROSAT PSPC images due to the low temperature sensitivity of the detector. The shocks also decelerate the gas, however, and cause the gas density distribution to differ from that of the dark matter. This process will lead to larger power ratios for the gas than for the dark matter. Competing with this effect is the fact that the gas in much of the main cluster as well as in the cores of infalling subclumps may be in or near hydrostatic equilibrium within the potential provided by the dark matter. Hydrostatic equilibrium causes the gas distribution to be more round than that of the dark matter, resulting in lower power ratios for the gas. Apparently this second effect is stronger, as we have shown that power ratios computed from the square of the dark matter density systematically overestimate the values based on the square of the gas density. A third effect which can separate the gas from the dark matter distributions, cooling, is only possible in the core of the cluster, where the power ratios are least sensitive.

Buote & Xu (1996) argue that using the square of the dark matter density as an approximation to the X-ray surface brightness is justified by Tsai & Buote (1996),

who computed power ratios for clusters in the hydrodynamic simulations of Navarro et al. (1995). However, Tsai & Buote only argue that the dark matter density (and not its square) gives power ratios that are qualitatively similar to those based on the square of the gas density. For example, for both the dark matter density and the square of the gas density, power ratios increase in response to mergers, then decay. However, Tsai & Buote do not address the issue of bias in the values of the dark matter power ratios, nor do they test the square of the dark matter density. Buote & Xu also take as support the fact that Jing et al. (1995) find similar centroid shifts and axial ratios for their simulated clusters when they assume gas traces dark matter and when they assume the gas is in hydrostatic equilibrium. In fact, Jing et al. only argue that axial ratios and centroid shifts have the same dependence on cosmological parameters regardless of which of these two prescriptions they apply for determining gas density from their N-body simulations. Jing et al. measure smaller statistics (indicating less substructure) when the gas is in hydrostatic equilibrium as compared to when the gas traces the dark matter. This is in agreement with our finding.

While significant statistically, this overestimate of power ratios by Buote & Xu is small enough that correcting for it does not greatly change their conclusions, but it does reduce the difference between their findings and those of Mohr et al. This correction, applied to the Buote & Xu power ratios, moves all the models tested by Buote & Xu, except for the open CDM model, into better agreement with the data. The best agreement is obtained with the $\Omega = 0.3, \Lambda = 0.7$ CDM model.

Chapter 5

An analytic model for predicting power ratios

Mohr et al. (1993) and Buote & Xu (1996) both tried to distinguish cosmological models by simulating many realizations of each model and comparing the distributions of their substructure statistics for the simulations to the same stastics applied to real clusters. This approach requires a large simulation effort to study each point in the space of cosmological parameters (Ω_M, Ω_Λ, H_0, $P(k)$). While much may be gained by studying a few selected cosmological models, we attempt instead to develop an analytical model which describes the merger events which result in high power ratios. While this model does require calibration against a simulation, it does not require a new batch of simulations for each model studied.

Richstone et al. (1992) and Lacey & Cole (1993) both used ad hoc estimates for the survival time of substructure. With a simple model we can connect the survival time to the substructure measurement in a self consistent way. Also, by isolating the elements which comprise the analytic model, we can subject each to individual study and improve the model assumption by assumption, element by element.

Several model elements go into estimating power ratios. This model requires knowledge of the merger rate as a function of time and of the two merging masses, the infall velocities of subclumps onto the main cluster, and the effect on the power ratios of a merger.

5.1 Merger rate

Most obviously, the distribution of observed power ratios must depend on the merger rate of the halos that make up a cluster of galaxies. Various authors have used extensions of the Press & Schechter (1974) formalism to compute merger probabilities (Bond et al. 1991), merger rates (Lacey & Cole 1993), merger histories (Kauffmann & White 1993) and related quantities from the linear power spectrum.

Following Lacey & Cole (1993), we consider $\delta(\vec{x})$, the initial overdensity field evolved linearly to the present. Smoothing $\delta(\vec{x})$ on a continuum of mass scales M gives a function $\delta(\vec{x}, M)$ which can be thought of, for each point $\vec{x}$, as a trajectory with $1/M$ in the role of the time variable.

$$\delta(\vec{x}, M) = \int_0^\infty \delta(\vec{x}')W(|\vec{x} - \vec{x}'|, M)d\vec{x}' \,. \tag{5.1}$$

The mass scale M is related to a length scale R by

$$M = \int_0^\infty \bar{\rho}W(r, M)4\pi r^2 dr \,. \tag{5.2}$$

As M and R approach infinity, the mean density enclosed in the smoothing volume approaches the cosmic mean, i.e., the overdensity $\delta(\vec{x}, M)$ approaches zero. As M is decreased, the mean density begins to vary. The character of these variations depends on the window function. The effect of different window functions on the trajectory of δ vs. M is explored in detail in Bond et al. (1991). Consider the case of the sharp k-space window function, for which the Fourier transform is

$$\hat{W}(k, R) = \vartheta(1 - kR) \tag{5.3}$$

and whose real space form is

$$W(r, R) = \frac{(\sin x - x\cos x)}{x^3}\left(\frac{1}{2\pi^2 R^3}\right), \tag{5.4}$$

where $x = r/R$. Expressing $\delta(\vec{x}, M)$ in terms of its Fourier components gives

$$\delta(\vec{x}, M) = \int_0^\infty \hat{\delta}(\vec{k})\hat{W}(k, M)\exp(\imath\vec{k}\cdot\vec{x})4\pi k^2 \frac{dk}{(2\pi)^3} \tag{5.5}$$

$$= \frac{1}{2\pi^2}\int_0^{1/R} \hat{\delta}(\vec{k})\exp(\imath\vec{k}\cdot\vec{x})k^2 dk\,, \tag{5.6}$$

where $\hat{\delta}(\vec{k})$ are the Fourier components of the unsmoothed density field. An decrease in smoothing mass scale corresponds to increasing the upper limit of the integral in Eq. 5.6. If the linear overdensity is a Gaussian random field, then its Fourier components $\hat{\delta}(\vec{k})$ are independent random variables, so increasing the integration limit means including more random variables in the integrand. As a result, the trajectory of $\delta(\vec{x}, M)$ is a random walk starting at zero for the largest M. As M is decreased, smaller volumes are averaged over and the fluctuations in $\delta(\vec{x}, M)$ increase.

Next, we include the spherical collapse model, which predicts a collapse time for a given spherical perturbation in an otherwise homogeneous universe (Gunn & Gott 1972). The equation of motion for a point a distance a from the center of such a perturbation is the Friedmann equation

$$\left(\frac{\dot{a}}{a}\right)^2 = H_0^2[\Omega_M a^{-3} + \Omega_\Lambda + \Omega_R a^{-2}]\,, \tag{5.7}$$

$$\Omega_M + \Omega_\Lambda + \Omega_R = 1\,, \tag{5.8}$$

where Ω_M, Ω_Λ and Ω_R are the fractions of the critical density in matter, vacuum energy, and curvature, respectively, all measured at the time corresponding to $a = 1$, and H_0 is the value of $\dot{a}/a$, also measured when $a = 1$. Ω_M is related to the overdensity δ by

$$\Omega_M = \frac{8\pi G\bar{\rho}(1+\delta)}{3H_0^2}\,. \tag{5.9}$$

If the matter density is sufficient, the perturbation's expansion will halt when $\dot{a} = 0$ and will collapse to zero size ($a = 0$) at twice that time, t_c, given by

$$H_0 t_c = 2\int_0^{a_{\max}} [\Omega_M a^{-1} + \Omega_\Lambda a^2 + \Omega_R]^{-\frac{1}{2}} da\,, \tag{5.10}$$

where $a_{\max}$ is the radius of maximum expansion and is the first real positive root of

$$\Omega_M + \Omega_\Lambda a^3 + \Omega_R a = 0\,. \tag{5.11}$$

For a given cosmological model Ω_Λ is constant but the matter density and hence the curvature vary spatially. We can therefore determine the collapse time for any spherical perturbation. Equivalently, for any time we can determine the linear overdensity of the perturbations which have just collapsed. We express this as a function $\delta_c(t)$, which can be thought of as a threshhold value applied to the smoothed linear overdensity field $\delta(\vec{x}, M)$. Clusters of mass M or greater have formed by time t wherever

$$\delta(\vec{x}, M) \geq \delta_c(t)\,. \tag{5.12}$$

Now reconsider the trajectories $\delta(\vec{x}, M)$ of the smoothed linear density field as M is decreased from infinity. At a fixed time t, the mass which has collapsed at $\vec{x}$ is equal to the largest mass for which $\delta(\vec{x}, M) = \delta_c(t)$, giving the distribution of cluster masses at t. This equation can also be used to give the evolution in time of collapsed mass at a fixed point $\vec{x}$. It is this latter application which can be extended to give merger rates and formation histories of collapsed halos.

In the case of sharp k-space filtering of the initial density field, the trajectory at fixed $\vec{x}$ is a random walk. It begins at zero for infinite M and random walks away. The probability density for the "distance walked," is a Gaussian (Chandrasekhar 1943, Bond et al. 1991),

$$P(\delta)d\delta = \frac{1}{\sqrt{2\pi\sigma^2}} \exp\Big(-\frac{\delta^2}{2\sigma^2}\Big)d\delta\,, \tag{5.13}$$

where $\sigma^2 = \sigma^2(M)$ is the variance in the smoothed field $\delta(\vec{x}, M)$. Each $\delta(M) > \delta_c(t)$ in the tail of the Gaussian corresponds to a mass point which has been incorporated into a cluster of mass M by time t. It crossed the boundary $\delta(M) = \delta_c(t)$ and continued to increase. For each trajectory that crosses and remains above $\delta_c(t)$ there is an equally likely one that crosses $\delta_c(t)$ at the same mass scale M but then decreases

as the mass scale is decreased and ends up below $\delta_c(t)$. These trajectories correspond to regions whose density is low on small scales but above the threshhold collapse density on larger scales, i.e., small underdense patches inside larger overdense ones. Despite being underdense on small scales, these have already been incorporated into larger mass objects. Hence, the probability that a mass point is in a collapsed object of mass M or greater at time t is equal to twice the area under the tail of the Gaussian above $\delta(M) = \delta_c(t)$. This is given by

$$P(> M, t) = 2 \int_{\delta_c(t)}^{\infty} P(\delta) d\delta \,. \tag{5.14}$$

Thus, the probability density for trajectories which have not crossed the $\delta_c(t)$ threshhold by time t is

$$P_{<\delta_c}(\delta) d\delta = \frac{1}{\sqrt{2\pi\sigma^2}} \Big\{ \exp\Big(-\frac{\delta^2}{2\sigma^2} \Big) - \exp\Big[-\frac{(\delta - 2\delta_c)^2}{2\sigma^2} \Big] \Big\} d\delta \,. \tag{5.15}$$

This is the solution to the diffusion equation

$$\frac{\partial P_{<\delta_c}}{\partial \sigma^2} = \frac{1}{2} \frac{\partial^2 P_{<\delta_c}}{\partial \delta^2} \,, \tag{5.16}$$

subject to an absorbing boundary condition at $\delta(M) = \delta_c(t)$. Trajectories start from $\delta = 0$ and "diffuse" outward, some eventually being "absorbed" when they reach $\delta_c(t)$ and collapse into objects of mass M.

As trajectories are absorbed into the density threshhold boundary, the probability density for trajectories which have not crossed the boundary decreases. Thus, the probability that a trajectory first crosses the threshhold $\delta_c(t)$ is

$$P(M, t) = -\frac{\partial}{\partial M} \int_{-\infty}^{\delta_c} P_{<\delta_c}(\delta) d\delta = -\frac{d\sigma^2}{dM} \frac{\partial}{\partial \sigma^2} \int_{-\infty}^{\delta_c} P_{<\delta_c}(\delta) d\delta \,, \tag{5.17}$$

which, by the diffusion equation, is

$$P(M, t) \;=\; -\frac{d\sigma^2}{dM} \frac{1}{2} \frac{\partial P_{<\delta_c}(\delta)}{\partial \delta} \Bigg|_{-\infty}^{\delta_c} \tag{5.18}$$

$$= -\frac{d\sigma^2}{dM}\frac{\delta_c}{\sqrt{2\pi}\sigma^3}\exp\Big(-\frac{\delta_c^2}{2\sigma^2}\Big)\,. \tag{5.19}$$

Recall that at fixed time t one determines the collapsed mass of an object by finding the largest mass scale for which $\delta(M) = \delta_c(t)$. Treating $1/M$ in the role of the time variable, and increasing $1/M$ from zero, then the first $1/M$ for which the threshhold is crossed determines the collapsed mass. The probability that a trajectory, which starts from the origin $\delta = 0$, crosses the collapse threshhold for the first "time" $(1/M)$ is then $P(M,t)dM$.

The probability of a mass point being in a collapsed object of mass M_1 at time t_1 provided it will be in an object of mass $M_2 > M_1$ at $t_2 > t_1$ is directly analogous to $P(M,t)$ just computed, but with the origin of the trajectory at "time" $1/M_2$ and $\delta = \delta_c(t_2)$.

$$P(M_1,t_1|M_2,t_2)dM_1 = \left|\frac{d\sigma_1^2}{dM_1}\right|\frac{\delta_1-\delta_2}{(2\pi)^{1/2}(\sigma_1^2-\sigma_2^2)^{3/2}}\exp\left[-\frac{(\delta_1-\delta_2)^2}{2(\sigma_1^2-\sigma_2^2)}\right]dM_1\,, \tag{5.20}$$

where $\delta_{1,2} = \delta_c(t_{1,2})$ and $\sigma_{1,2} = \sigma(M_{1,2})$. This equation can be used to give the mass distribution of precursors to the mass M_2.

We can also compute the probability that a mass point that is already in a collapsed halo of mass M_1 at time t_1 will collapse into a larger mass halo M_2 at a later time t_2. This is determined by

$$P(M_2,t_2|M_1,t_1)dM_2 \times P(M_1,t_1)dM_1 = P(M_1,t_1|M_2,t_2)dM_1 \times P(M_2,t_2)dM_2\,, \tag{5.21}$$

which yields

$$P(M_2,t_2|M_1,t_1)dM_2 = \left|\frac{d\sigma_2^2}{dM_2}\right|\frac{1}{(2\pi)^{1/2}}\frac{\delta_2\sigma_1^3}{\delta_1\sigma_2^3}\frac{\delta_1-\delta_2}{(\sigma_1^2-\sigma_2^2)^{3/2}}\exp\left[-\frac{(\delta_2\sigma_1^2-\delta_1\sigma_2^2)^2}{2\sigma_1^2\sigma_2^2(\sigma_1^2-\sigma_2^2)}\right]dM_2\,. \tag{5.22}$$

In the limit as t_2 approaches t_1, any finite change in mass must be the result of a merger rather than continous accretion. As the time dependence in equation 5.22 is contained entirely in the $\delta_{1,2} = \delta_c(t_{1,2})$ terms, this limit is equivalent to the limit as

$\delta_2 \to \delta_1 = \delta_c(t)$, which gives

$$\frac{d^2P}{d\Delta M dt} = \frac{1}{2\pi}\left[\frac{\sigma_1^2}{\sigma_2^2(\sigma_1^2-\sigma_2^2)}\right]^{3/2} \exp\left[-\frac{\delta_c^2(t)}{2}\left(\frac{1}{\sigma_2^2}-\frac{1}{\sigma_1^2)}\right)\right]\left|\frac{d\sigma_2^2}{dM_2}\right|\left|\frac{d\delta_c}{dt}\right| \tag{5.23}$$

This expression is equivalent to Eq. 2.18 of Lacey & Cole (1993). In a subsequent paper, Lacey & Cole (1994) tested this expression and the related predictions for the halo mass function and halo formation times against N-body simulations of scale-free models and found very good agreement. This should not be surprising, as it is common practice among N-body simulators to compare their mass function with the Press & Schechter (1974) formula and to find reasonable agreement (Efstathiou et al. 1988, Efstathiou & Rees 1988, White, Efstathiou & Frenk 1993, Bond & Myers 1993).

Equation 5.23 tells us the merger rate. We also need to model what occurs during these mergers in order to predict the power ratios.

5.2 Infall model

Close inspection of the cluster simulation reveals that most high power excursions in power ratio space correspond to single merger events in which a subclump of dark matter and hot gas falls onto the main cluster. The power ratios (especially P_2/P_0) begin to rise when the subclump starts to cross the aperture within which the power ratios are computed. As these mergers are almost always radial or nearly so, the power ratio decays away as the clump falls inside the aperture. The radial nature of the orbits is a common feature in hierarchical clustering simulations, as clumps form in sheets and filaments, then are funnelled along the filaments into the knots where the filaments intersect and the clusters form.

We model these mergers as the collision between two point masses on a radial orbit. This model is best known for its application to the Local Group, in which M31 and the Milky Way are treated as point masses. The observed distance and infall velocity of M31 with respect to the Milky Way are combined with estimates of the

age of the Universe to compute the mass of the Local Group. The equation of motion for the problem of two point masses interacting gravitationally is

$$\frac{d^2\vec{r}}{dt^2} = -\frac{GM}{r^3}\vec{r}, \tag{5.24}$$

where $\vec{r}$ is the separation vector between the two masses and M is the sum of the two masses. The general solution for $r = |\vec{r}|$ for an orbit with eccentricity e is given parametrically in terms of the eccentric anomaly η,

$$r = A(1 - e\cos\eta), \tag{5.25}$$

$$t = B(\eta - e\sin\eta), \tag{5.26}$$

$$A^3 = GMB^2. \tag{5.27}$$

Because the orbits we observe in the simulation are radial or nearly so, we henceforth set $e = 1$.

Denote the collision time of these two masses as T. The probability density for such a merger is given in Eq. 5.23, changing the variable t to T to avoid confusion with the time coordinate in the two body problem solution, Eq. 5.26. The probability that a merger of masses M and ΔM occurs between the times T and $T + dT$ is $(d^2P/d\Delta M dT)dT$. The probability that, during the time interval from t to $t + dt$, masses M and ΔM will be separated by a distance R and on their way to a merger at time T is then $(d^2P/d\Delta M dT)(dT/dt)_r dt$.

$$\left(\frac{dT}{dt}\right)_r = \left(\frac{dT}{d\eta}\right)_r \left(\frac{dt}{d\eta}\right)_r^{-1}, \tag{5.28}$$

with the subscript r denoting that all derivatives are taken at fixed r. Collision occurs when $r = 0$, or $\eta = 2\pi$, so $T = 2\pi B$, and

$$r = \left(\frac{GMT^2}{4\pi^2}\right)^{1/3}(1 - \cos\eta) \tag{5.29}$$

$$= (GMt^2)^{1/3}\frac{1 - \cos\eta}{(\eta - \sin\eta)^{2/3}}. \tag{5.30}$$

Using Eqs. 5.29 and 5.30 we find that at fixed r,

$$dr = \left(\frac{GM}{4\pi^2}\right)^{1/3}\left[(1-\cos\eta)\frac{2}{3}T^{-1/3}dT + T^{2/3}\sin\eta\, d\eta\right] = 0 \tag{5.31}$$

$$= (GM)^{1/3}\left\{\frac{1-\cos\eta}{(\eta-\sin\eta)^{2/3}}\frac{2}{3}t^{-1/3}dt + \right. \tag{5.32}$$

$$\left. t^{2/3}\left[\frac{\sin\eta}{(\eta-\sin\eta)^{2/3}} - \frac{2}{3}\frac{(1-\cos\eta)^2}{(\eta-\sin\eta)^{5/3}}\right]d\eta\right\} = 0\,, \tag{5.33}$$

so that

$$\left(\frac{dT}{d\eta}\right)_r = -\frac{3}{2}T\frac{\sin\eta}{1-\cos\eta} \tag{5.34}$$

$$\left(\frac{dt}{d\eta}\right)_r = -\frac{3}{2}t\left(\frac{\sin\eta}{1-\cos\eta} - \frac{2}{3}\frac{1-\cos\eta}{\eta-\sin\eta}\right). \tag{5.35}$$

Eq. 5.28 then yields

$$\left(\frac{dT}{dt}\right)_r = \frac{2\pi\sin\eta}{\eta\sin\eta - \sin^2\eta - \frac{2}{3}(1-\cos\eta)^2}\,. \tag{5.36}$$

This quantity ranges from zero at $\eta = \pi$ to one at $\eta = 2\pi$, though in practice it is never far from unity. We can now compute $(d^2P/d\Delta M dT)(dT/dt)_r dt$, the probability of masses M and ΔM at separation r in the time interval $(t, t+dt)$, on their way to merge at time T.

The next model element required is the duration the mass ΔM spends near the image aperture radius, where it contributes strongly to high power ratios. Again, we employ the solution to the 2 body problem. At time t the relative velocity of the two masses is

$$v = \frac{dr}{dt} = \left(\frac{dr}{d\eta}\right)\left(\frac{dt}{d\eta}\right)^{-1}, \tag{5.37}$$

which, according to Eqs. 5.25 and 5.26 is

$$v = \frac{A\sin\eta}{B(1-\cos\eta)} = \left(\frac{GM}{r(1-\cos\eta)}\right)^{1/2}\sin\eta\,. \tag{5.38}$$

The amount of time the subclump ΔM spends crossing the image aperture is just

the size of the subclump divided by its infall velocity. The size of the clump can be estimated as the radius of a sphere with 200 times the critical density which contains mass ΔM,

$$\Delta M = \frac{4\pi}{3} R_{\Delta M}^3 (200\rho_{\rm crit}) = 200\frac{R_{\Delta M}^3 H^2}{2G}\,. \tag{5.39}$$

While this choice may seem *ad hoc*, our results will not be sensitive to it. This is because any linear error will be calibrated away when the model predictions are compared to the simulation. Non-linear variation in halo size as a function of mass would manifest itself as a variation in the halo's concentration, a measure of how strongly the mass is concentrated. Detailed work on the structure of dark matter halos by Navarro et al. (1996) shows that variations in concentration with mass are extremely small. The time for subclump ΔM to fall through an aperture of radius $R_{\rm ap}$ is then approximately

$$t_{\rm fall} = 2R_{\Delta M}/v\,. \tag{5.40}$$

A more rigorous derivation of the subclump infall time, based on the infall solution for the two body problem, is as follows. Let t_1 be the time at which the subclump edge first touches the aperture on its way in. This occurs when the separation of the two components is $r_1 = R_{\rm ap} + R_{\Delta M}$. Let t_2 be the time at which the subclump comes completely within the aperture. In the limit of small ΔM, this occurs at $r_2 = R_{\rm ap} - R_{\Delta M}$. However, for large ΔM we must account for the shift of the aperture center. Recall that the aperture center is found by minimizing the difference the center of the aperture and the emission weighted centroid of the portion of the image within the aperture. For the two body model, this is equivalent to the center of mass. When the separation of the subclump and the main halo is more than $R_{\rm ap}$, the aperture sits centered on the main halo. As the subclump enters the aperture, the aperture center shifts to the center of mass of the pair. As a result, the merger ending time t_2 occurs when

$$r_2 = (R_{\rm ap} - R_{\Delta M})\left(1 + \frac{\Delta M}{M + \Delta M}\right). \tag{5.41}$$

The corresponding times $t_{1,2}$ can be found by solving equation 5.25 for $\eta_{1,2}$, then using equation 5.26 to solve for $t_{1,2}$. The difference in these times is the duration of the merger,

$$t_{\rm fall} = t_2 - t_1 \,. \tag{5.42}$$

This determination of $t_{\rm fall}$ is not very different from equation 5.40, especially for small ΔM, but as it is more consistent with the infall model we will use it hereafter.

Our definition of $t_{\rm fall}$ depends on the simple radius - mass relationship for the subclump, equation 5.39. As mentioned in the discussion following that equation, much of any error in $t_{\rm fall}$ introduced by that simple relationship can be calibrated away using a simulated merger. We choose the merger corresponding to the high power excursion occurring near redshift $z = 2.5$. For this event, the model predicts an infall time $t_{\rm fall} = 0.39$ Gyr. The full width at half maximum for the P_2/P_0 peak, seen in figure A-13, is about 0.13 Gyr. Henceforth then, we shall renormalize $t_{\rm fall}$ by the factor $0.13/0.39 = 1/3$. This is roughly equivalent to assuming that the subclump radius is smaller than that given by equation 5.39 by the same factor. This is not surprising, as the subclumps are expected to be centrally concentrated rather than uniform density, as equation 5.39 assumes. A factor of three reduction in radius corresponds to a factor of $3^3 = 27$ increase in density, and in fact the subclump here has a density contrast of about 10,000 at $R_{\Delta M}/3$. While a more precise estimate of the infall time may be obtained through more sophisticated modelling of the subclump structure, furher accuracy is not required here. Below, when the power ratio estimates are computed, we shall see that the factor of $1/3$ normalization used here can be subsumed into another normalizing factor required then.

Calculating the model prediction $t_{\rm fall}$ for our simulated cluster, we find that the infall time varies by less than a factor of two for fixed $\Delta M/M$ from redshift $z = 3$ to $z = 1$, and by a similarly small factor in the range $0.1 \leq (\Delta M/M) \leq 1.0$ at fixed redshift. The infall times increase gradually with time, as the main cluster mass also increases. This model prediction can be seen in table 5.1, which shows for each redshift the main cluster mass M at that redshift and the infall time $t_{\rm fall}$ for subclumps

z	$M/M_\odot$	$t_{\rm fall}(\Delta M/M = 0.1)$	$t_{\rm fall}(\Delta M/M = 1.0)$	$t_{\rm cross}$	$t_{\rm dyn}$
3	3.2×10^{13}	0.086	0.137	0.287	1.163
2	5.7×10^{13}	0.115	0.181	0.326	1.123
1	1.3×10^{14}	0.158	0.240	0.417	1.096

Table 5.1: Model predicted $t_{\rm fall}$ for simulated cluster

of mass $0.1M$ and $1.0M$. This predicted trend is followed by the simulated cluster, as is evident in figures A-13, A-14 and A-15. These show the gradual widening of peaks in the power ratios, corresponding to increasing $t_{\rm fall}$, as time increases and the cluster grows.

Our $t_{\rm fall}$ can be compared to the estimates for substructure survival time used by Richstone et al. (1992) and others. The dynamical time for a cluster is

$$t_{\rm dyn} = (G\rho)^{-1/2}\,, \tag{5.43}$$

and the crossing time is

$$t_{\rm cross} = r/(\sqrt{3}\sigma_c)\,, \tag{5.44}$$

where σ_c is the velocity dispersion within the cluster.

These have been computed for the simulated cluster using the velocity dispersion of the dark matter particles to compute the crossing time and using the mean mass density within the aperture to compute the dynamical time. Values are given in table 5.1. Again we see that the estimates of substructure survival time assumed by Richstone et al. (1992) and Lacey & Cole (1993) are too high, at least as applied to the survival time of high power ratios.

The crossing time $t_{\rm cross}$ is the timescale for the subclump to cross the aperture. But it never does that. For apertures of 0.5 Mpc and greater, the subclump typically loses enough kinetic energy, by dynamical friction as well as by the drag force on the gas, such that even if it doesn't merge with the main cluster immediately, it will never recede out to the aperture radius again. And since the power ratios disappear as the subclump approaches the center of the main cluster, the power ratios are only

high while the subclump passes through the aperture on infall. From this argument, we can see that dividing the crossing times in half brings them into the same range as $t_{\rm fall}$.

The dynamical time $t_{\rm dyn}$ may be the appropriate survival time for a subclump orbiting in the dense cluster environment, but it is much longer than the time required for the infalling subclump to cross the aperture.

5.3 Power ratio prediction

Combining the merger rate and infall model, equations 5.23, 5.36 and 5.42 give

$$\frac{dP}{d\Delta M} = \frac{d^2P}{d\Delta M dT}\left(\frac{dT}{dt}\right)_r t_{\rm fall}\,, \tag{5.45}$$

which is the probability density for the power ratios to be high due to an imminent merger with a subclump of mass ΔM.

The expectation value for the power ratios of a cluster of a specified mass can now be computed if we add to our model an estimate of the power ratios as function of the two merging masses. Since our model assumes spherical masses on a radial orbit, we will concentrate on P_2/P_0.

According to equation 4.15,

$$\frac{P_2}{P_0} = \frac{(a_2^2+b_2^2)}{a_0^2}\frac{1}{8R_{ap}^4(\ln R_{ap})^2}\,, \tag{5.46}$$

where a_2 and b_2 are given by equations 4.13. To facilitate comparison with Buote & Xu (1996), we set the scale of the power ratios by choosing kiloparsecs as the units for R_{ap}. For two masses approaching along a line, we can orient our coordinate system to eliminate b_2, leaving

$$\frac{P_2}{P_0} = \frac{\left[\int_{r\le R_{ap}}\Sigma(r,\phi)r^2\cos 2\phi\ \ rdrd\phi\right]^2}{\left[\int_{r\le R_{ap}}\Sigma(r,\phi)\ \ rdrd\phi\right]^2}\frac{1}{8R_{ap}^4[\ln(R_{ap}/1{\rm kpc})]^2}\,. \tag{5.47}$$

The simplest model we can take for the X-ray surface brightness Σ is to assume a point mass with luminosity proportional to mass. Labelling the subclump mass ΔM and the main cluster mass M, and the distance of each from aperture center as r_1 and r_2, respectively, we have

$$\frac{a_2}{a_0} = \frac{Mr_1^2 + \Delta M r_2^2}{\Delta M + M}. \tag{5.48}$$

Because the aperture is defined to be the center of emission, here it is the center of mass, so $Mr_1 = \Delta M r_2$, and

$$\frac{a_2}{a_0} = \left(\frac{M(\Delta M/M)^2 + \Delta M}{M + \Delta M}\right) r_2^2. \tag{5.49}$$

Because the power ratios peak when the subclump is just at the aperture radius, we take $r_2 = R_{ap}$. This yields

$$\frac{P_2}{P_0} = \left(\frac{M(\Delta M/M)^2 + \Delta M}{M + \Delta M}\right)^2 \frac{1}{8[\ln(R_{ap}/1\mathrm{kpc})]^2}, \tag{5.50}$$

which we take as our estimate of the power ratio P_2/P_0 as the subclump mass ΔM falls through the aperture onto the main cluster mass M.

Although we included the factor of $8[\ln(R_{ap}/1\mathrm{kpc})]^2$ in the P_2/P_0 estimate, we expect that the point mass approximation used to estimate a_2/a_0 is sufficiently inaccurate that a further calibration step is necessary. Using the same merger event for which we calibrated t_{fall}, we find that the predicted $\log(P_2/P_0)$ for this event, given the mass of the cluster and subclump and the time of the merger, is -3.35, much larger than the measured value of -4.46. This measurement is obtained from the projected square of the dark matter density, as done by Buote & Xu (1996), as we will be comparing to their data below. This means that for this particular merger, the value of P_2/P_0 predicted by our model is almost 13 times larger than for the simulated event. While it is hard to say how reasonable this factor is without more complex modelling of the merger, we are not surprised that the predicted value is high compared to the actual value. The matter distribution in each cluster compononent is of course not

that of a point mass, and a more smeared out matter distribution will give rise to a smaller P_2/P_0. In addition, we have assumed in our model that the power ratios peak when the subclump is exactly at the aperture edge. While this is true for a point mass, an extended mass will not contribute fully to the power ratios until most of it has passed within the aperture, i.e., until its center is somewhat within the aperture. This means that a more sophisticated model should use $r_2 < R_{ap}$ in equation 5.48, resulting in a lower predicted P_2/P_0 in better agreement with the simulation. In order to account for this oversimplification of the merger model, we henceforth renormalize the predicted P_2/P_0 by dividing by 12.88, the exact value of the model overestimate.

Combined and integrated over, equations 5.45 and 5.50 give the expectation value of P_2/P_0 for a cluster of mass M:

$$\left\langle \frac{P_2}{P_0} \right\rangle = \int_{fM}^{M} \frac{dP}{d\Delta M} \frac{P_2}{P_0} d\Delta M \,. \tag{5.51}$$

The upper limit of integration is M, so that this integral only counts mergers inwhich the subclump is less massive than the main cluster. This prevents double counting. The factor f in the lower limit of the integral is the fractional mass of the smallest subclump to include in the integral. In practice the value $f = 0.01$ was sufficient for the integral to converge. Lower mass subclumps, while common, do not make a significant contribution to the power ratios.

We compared this model prediction to our simulated cluster. At redshifts of 4, 3, 2.5, 2, and 1, we applied the DENMAX algorithm to the simulation outputs to determine the main cluster mass at these epochs. For each, we evaluated equation 5.51 to determine the expected power ratio P_2/P_0. These values are plotted in figure A-9. Of course, our single cluster is free to deviate from the mean cluster prediction, but it is reassuring that the general trend of a slowly decreasing P_2/P_0 with increasing time (and cluster mass) is common to both the simulation and the model prediction.

Equation 5.51 gives the mean P_2/P_0 for clusters of mass M. In order to determine the mean P_2/P_0 for the ensemble of clusters in a given cosmological model, we need the cluster mass function. Equation 5.19 gives the probability for a mass point to

collapse into a mass M at time t. Multiplying by ρ_0/M then gives the differential number density of collapse objects, i.e., the mass function,

$$\frac{dn}{dM}(M,t)dM = \frac{1}{(2\pi)^{1/2}}\frac{\rho_0}{M}\frac{\delta_c(t)}{\sigma^3(M)}\left|\frac{d\sigma^2}{dM}\right|\exp\left[-\frac{\delta_c^2(t)}{2\sigma^2(M)}\right]dM\,. \tag{5.52}$$

The ensemble mean of the log of the power ratio P_2/P_0 is then given by

$$\left\langle \log\left(\frac{P_2}{P_0}\right)\right\rangle_{\text{ensemble}} = \frac{\int_M^{fM}\log\left(\left\langle\frac{P_2}{P_0}\right\rangle\right)\frac{dn}{dM'}(M',t)dM'}{\int_M^{fM}\frac{dn}{dM'}(M',t)dM'}\,, \tag{5.53}$$

where the factor f in the upper integration limit should be set to about 100 for convergence. The lower limit M is now the minimum mass cluster to include in the power ratio averaging. In comparing to real data this would be the lower mass limit of a mass limited cluster sample, if such a thing were possible.

Note that two components of the expression for the ensemble mean of the logarithm of P_2/P_0 have been calibrated with our simulation. The merger timescale t_{fall} predicted by the infall of two point masses was rescaled by a factor of 1/3. This factor enters equation 5.53 through the merger rate, given by equation 5.45. Then the expression for the power ratio P_2/P_0 for a merger of two given masses (equation 5.50) was rescaled by a factor of 1/12.88. Since these two expressions are multiplied in the integrand for the ensemble average P_2/P_0, given by equation 5.53, they amount to only a single free parameter.

5.4 Testing the predictions

We can compare these power ratio predictions to the mean power ratios presented by Buote & Xu (1996). They performed large N-body simulations of several cosmological models and extracted clusters from each. Projections of the square of the dark matter density were constructed for each cluster, and the power ratios were computed from those images. Each of their models was evolved in a $200h^{-1}$ Mpc box, with the same set of random phases in the initial conditions, from which they extracted the 39

Model	Ω_m	Ω_Λ	H_0	σ_8	$M_{\rm low}$	$\log(P_2/P_0)_{\rm ensemble}$	$\log(P_2/P_0)_{\rm BX}$
SCDM	1	0	50	1.00	3.61×10^{15}	-6.09 ± 0.20	-5.38 ± 0.76
OCDM	0.35	0	70	0.79	6.35×10^{14}	-6.03 ± 1.12	-5.93 ± 1.03
LCDM	0.35	0.65	70	0.83	7.17×10^{14}	-6.13 ± 1.10	-5.87 ± 0.83

Table 5.2: Buote & Xu (1996) simulation model parameters with measured and model predicted P_2/P_0

largest clusters in each. Our comparison requires determining the model prediction for the average P_2/P_0 for the 39 largest clusters in each model. For this we must first determine the lower limit $M = M_{\rm low}$ to use in equation 5.53. Since Buote & Xu use their 39 largest clusters in a $200h^{-1}$ Mpc box, we must do likewise for our comparison. We determine $M_{\rm low}$ by solving the equation

$$\int_{M_{\rm low}}^{\infty} \frac{dn}{dM'}(M', t_0) dM' = \frac{39}{(200h^{-1}{\rm Mpc})^3}, \tag{5.54}$$

which is just the denominator in equation 5.53.

Table 5.2 gives the three models for which we compare our model predictions to the simulation data of Buote & Xu (1996). The model parameters Ω_M, Ω_Λ, H_0 and power spectrum normalization σ_8 are given for the "Standard" CDM model (SCDM), an open CDM model (OCDM), and a low density flat model with cosmological constant (LCDM). In each case the power spectra are given by Bardeen et al. (1986). Also listed in the table is the mass of the least massive cluster in the comparison $M_{\rm low}$, followed by the model predicted value and the simulated value for the mean of the decimal logarithm of P_2/P_0, denoted $\log(P_2/P_0)_{\rm ensemble}$ and $\log(P_2/P_0)_{\rm BX}$, respectively. The variances of these last two quantities are also given.

Most obvious in this comparison are the low predictions for the power ratios. The under-prediction is most severe for the SCDM model, while the OCDM prediction is fairly good. What are the possible causes of this under-prediction? One obvious possibility is that our calibration event may have been atypical in some way. Recall that we used a merger which occurred at $z = 2.5$, in which the main cluster of mass $4.7 \times 10^{13} M_\odot$ merges with a subclump of approximately 1/3 of that mass. In separate

stages we calibrated first the subclump infall time $t_{\rm fall}$, then the predicted power ratio P_2/P_0. Although this was done in two stages, the net result for the prediction of the ensemble mean P_2/P_0 is that there is only one free parameter, which is the product of the two calibration factors described above. If the chosen calibration event occurred faster than is typical of similar mergers then the calibration factor applied to $t_{\rm fall}$ was too small and should be increased. If the calibration event gave a measured P_2/P_0 which was lower than everage for such events, then the factor applied to P_2/P_0 was likewise too small. Either or both of these would cause the predicted power ratios to be too low.

In order to investigate this possibility, we would like to have several more calibration points. Unfortunately this is not presently possible. The next candidate event for use as a possible calibrator is the merger that occurs just after $z = 2$ ($a = 0.34$ in figures A-4, A-5 and A-6). However, as is evident in these figures, this is not as well isolated an event as that at $z = 2.5$ ($a = .28$). This means that we can expect that the measured P_2/P_0 is a result of several nearly coincident mergers rather than one larger event. Inspection of the positions and masses of clumps in the dark matter particle distribution of the simulation confirms this. There are several small clumps, each with about one tenth the mass of the central cluster, falling together at this time. From this it is impossible to draw out the effect of a single subclump on the power ratios. Since our model effectively treats this situation as a combination of many simpler events, rather than a single multi-component merger, this event will not serve as a reliable calibration point. Note also that almost all the other peaks in the power ratios are much lower than that at $z = 2.5$. Since we expect the calibration to be most accurate when the calibration event clearly involves two dominant components, these lower power events will not serve. Finally, we choose not to use the merger at $z \approx 5.5$ ($a \approx 0.18$) as the cluster mass at this time is only $2 \times 10^{13} M_{\odot}$. This is much smaller than the mass of the least massive cluster for which we are making the comparisons in table 5.2. In fact, this is also true of the merger at $z = 2.5$ which we used as our calibration event. The mass difference then between the calibration event and the comparison events may account for some of the underestimate in the power

ratio predictions. Ideally we would have prefered to have many calibration merger events with masses in the range for which we make our comparisons. Although this is unavailable in our current simulation, this calibration data would be easily available from gasless N-body simulations with lower mass and force resolution.

Another possible source of the under-predictions of P_2/P_0 given by equation 5.53 is in the mass function, which we take from equation 5.52. Differences between the theoretical and simulated mass functions could skew the predicted power ratios. For example, if the predicted dn/dM is too high, then the lower mass limit $M_{\rm low}$ determined from equation 5.54 will be too high also. Because P_0 is large for massive clusters, the mean P_2/P_0 at a given mass is a declining function of mass, so that the most massive clusters have low power ratios. Using a high value for $M_{\rm low}$ then excludes high power ratio clusters from the ensemble average. Also, if dn/dM as predicted by equation 5.52 is too shallow at the high mass end, as compared to the simulated clusters of Buote and Xu (1996), then the ensemble average in equation 5.53 will give too much weight to the most massive clusters. A too-shallow mass function then will result in a too-low ensemble average P_2/P_0.

The predictions of the Press & Schechter (1974) mass function (equation 5.52) have been tested against simulations, with generally good agreement (Efstathiou et al. 1988, Efstathiou & Rees 1988, White, Efstathiou & Frenk 1993, Bond & Myers 1993). This mass function goes from a power law at low mass to an exponential cut-off at high mass, with the transition mass M_* more than an order of magnitude less than the lowest mass cluster $M_{\rm low}$ in our comparison. Most of the work done in studying the mass function concentrates on the region from the low mass end to perhaps one order of magnitude above M_*, which means the mass function has not been tested in this regime. While the success of the predicted mass function in the low mass regime is reassuring, its application in the high mass regime is still uncertain. As a result, errors here could be partly to blame for our model's low power ratio estimates. While errors in the normalization of the mass function may be significant, errors in its shape can have only a small effect. We computed the expected value of P_2/P_0 for clusters of mass $M_{\rm low}$ for each cosmological model (equation 5.51) and found that this value

was already significantly less than the Buote & Xu average values. This means that over the whole mass range of our comparison, $M_{\rm low}$ and above, the expectation value of P_2/P_0 is low. While an overestimate of the mass function at the high mass end may cause a significant underestimate of the power ratios, any additional effect due to error in the shape of the high end of the mass function is small.

Another problem evident in the model predictions for P_2/P_0 is that the predicted values are much closer together than are those from the simulations, and the relative order of the power ratios is different. I.e., for these cosmological models the ensemble mean values of the power ratios span only a small range, and the OCDM model is predicted to have the highest power instead of the SCDM model. By studying different factors in the model prediction, we can determine at least part of the explanation for the small range of predicted P_2/P_0 over these three models.

One such factor is their power spectra, $P(k)$, which are plotted versus wavenumber k in figure A-21. The two low density models have nearly identical power spectra, while the SCDM model has significantly higher power on cluster and lower mass scales. We saw a manifestation of this in table 5.2, in which the mass $M_{\rm low}$, which is basically the mass of the 39th largest cluster, is much larger for the high density SCDM model than for the low density models. In other words, the SCDM model produces more rich clusters at a given mass scale.

Most of the factors going into the power ratio prediction are functions of the power spectrum through σ^2, so these factors are quite similar for the OCDM and LCDM models. One difference between these two, however, is in the age of the Universe. Note the factor of $1/t$ in the expression (equation 5.45) for the merger rate. Now consider realizations of the LCDM and OCDM models, using the same random numbers to generate the phases in the initial density field. Since the power spectra are so similar, the number of clusters and the number of mergers which take place from $t = 0$ to the present will be about the same in both models. Thus the younger model has a higher merger rate. This is the $1/t$ dependence. The age of the OCDM model is 11.1×10^9 years, and that of the LCDM model is 12.9×10^9 years. This age difference results in the prediction for the ensemble average of the log of P_2/P_0 being 0.07 lower for

LCDM than if the two model universes were the same age. This is the dominant factor in the difference between the two low density models.

In the Buote & Xu data, the OCDM and LCDM clusters show similar power ratios, while the SCDM power ratios are higher. The reason this is not the case for the power ratio predictions is primarily due to the $d\sigma^2/dM$ term in the merger rate equation (5.45). This term is lower for SCDM than for the open models by a factor of about 4. We can see the reason for this by considering $d\sigma^2/dM$ for a power law model, for which

$$\frac{d\sigma^2}{dM} = -\frac{3+n}{n}\frac{\sigma^2}{M}, \tag{5.55}$$

where n is the power law index for the power spectrum $P(k) \propto k^n$. Although the effective power law index on cluster scales differs for these three models, by far the greater difference is in the mass scales. $M_{\rm low}$ for the SCDM model is 5-6 times larger than for the low density models. σ_2 for the SCDM model is larger than for the others, but not by enough to make up for the difference in the mass scales. Another factor of two difference between the SCDM predictions and those for the other models comes from the $\sigma_1^2/\sigma_2^2(\sigma_1^2 - \sigma_2^2)$ term.

We should also note that although the Press & Schechter (1974) mass function has been tested and found generally successful, we are testing it severely. By focusing on rich clusters, we deal only with the high mass end of the mass function, where it drops off exponentially with mass. Tests of the mass function using N-body simulations have not focused on this regime, due to the small numbers of such rare events. In addition, several authors (Bond et al. 1991; Efstathiou & Rees 1988; Carlberg & Couchman 1989; Bond & Myers 1993) have investigated the effects of using different window functions, different values for the critical density for collapse δ_c, and even different methods for identifying collapsed objects in the simulations they use in their tests. It may be that such a modification could improve the accuracy of the high mass cutoff in the mass function. As a crude test of such a possibility, we tried adjusting the collapse density δ_c by 20% in either direction. This resulted in only a 1% change in the predicted power ratio.

Extensions to the Press & Schechter formalism have also been tested. Specifically, Lacey & Cole (1994) used N-body simulations of scale free models to test their merger rate formula (equation 5.45). Kauffmann & White (1993) developed a Monte Carlo approach for constructing merger histories of clusters and compared the results to a CDM simulation. Both of these groups report good agreement. Because we use their formula for the merger rate, the Lacey & Cole tests are most relevant to our work. Unfortunately, they did not explicitly test CDM models, but instead tested scale free models and argued that the good agreement found there should hold for CDM models as well. We also expect a similar level of accuracy for CDM models as for scale free models, as our tests rely only on a relatively narrow range of mass scales, i.e., those relevant to rich clusters.

Other factors which may share the blame for the SCDM predictions being too low relative to the other two models include those factors discussed above, such as the accuracy of the high end of the mass function. Also, the value of P_2/P_0 for a given merging pair (equation 5.50) may need to include a more complicated dependence on the masses or on the background density. Similarly, the simple two point mass solution may need to be modified to include a more complicated dependence on the masses.

It seems that the cosmological model discriminating power of the power ratios is not realized by our simple analytic model. Our model and the simulations of Buote & Xu (1996) are consistent in their predictions for the dependence of the power ratios on the cosmological constant Λ. Both show clearly that the mean power ratios are not sensitive to Λ. In our predictions for sensitivity to Ω, however, we and Buote & Xu strongly disagree. Figure A-20 shows the very slight dependence we find on both Λ and Ω. In this figure we compare the model predictions for P_2/P_0 as a function of Ω for open and flat cosmological models. All of these models are normalized to $\sigma_8 = 0.6$, so that all have similar cluster abundances. The variation in mean power ratio predictions with Ω is much less than the typical variance, as given for the model and the simulations of Buote & Xu in table 5.2.

Why do Buote and Xu find an Ω dependence of a factor of three between SCDM

and the low density models? We have isolated many of the factors which could contribute to such a dependence, and we have found none related to the merger rate. The subclump infall time varies by at most a factor of two between small and large infall masses for a given model and cluster mass, and varies by much less across models for reasonable cluster masses. Even if the two body orbit is a poor approximation to subclump infall, it seems unlikely that SCDM subclumps take three times as long as OCDM or LCDM subclumps to fall onto the cluster. The likely culprit, then, is in the assumption of point masses in the estimate of P_2/P_0 for a given merger event (equation 5.50). Perhaps a more realistic mass distribution would illuminate an Ω dependence.

To test this hypothesis, we computed the integrals for a_2 and a_0 (equation 4.12) while modelling the subclump halo as having constant surface density within the radius $R_{\Delta M}$. The integration is over the area in which the image aperture and subclump disk overlap.

The following definitions are useful.

$$A(R,r,d) = \frac{1}{2}R^2\theta(R,r,d) - R^2\cos\theta(R,r,d)\sin\theta(R,r,d) \tag{5.56}$$

$$\cos\theta(R,r,d) = \frac{d^2+R^2-r^2}{2dR} \tag{5.57}$$

$$F_0(R,r,d) = \begin{cases} A(R,r,d) + A(r,R,d) & \text{if } d^2 \geq r^2+R^2 \\ \pi r^2 + A(R,r,d) - A(r,R,d) & \text{if } d^2 < r^2+R^2 \\ \pi r^2 & \text{if } d+r \leq R \\ 0 & \text{if } d \geq R+r \end{cases} \tag{5.58}$$

$$\begin{aligned} F_1(R,r,d) = \; & \tfrac{R^2-d^2-r^2}{4d}\sqrt{4d^2r^2-(R^2-d^2-r^2)^2} \\ & + r^2 d\left[\arcsin\left(\tfrac{R^2-d^2-r^2}{2rd}\right) + \tfrac{\pi}{2}\right] \end{aligned} \tag{5.59}$$

$$F_2(R,r,d) = d \times F_1(R,r,d) \tag{5.60}$$

Utilizing these definitions, and modelling the subclump of mass ΔM as a uniform

disk of radius $R_{\Delta M}$ and surface density $\Delta M/(\pi R_{\Delta M}^2)$,

$$a_0 = M + \frac{\Delta M}{\pi R_{\Delta M}^2} F_0(R_{\rm ap}, R_{\Delta M}, d_2) \tag{5.61}$$

$$a_2 = M d_1^2 + \frac{\Delta M}{\pi R_{\Delta M}^2} F_2(R_{\rm ap}, R_{\Delta M}, d_2)\,. \tag{5.62}$$

Here $d_{1,2}$ are the distances from the image center to the centers of the main cluster and subclump, respectively, and

$$d_1 = \frac{\Delta M}{M} \frac{F_1(R_{\rm ap}, R_{\Delta M}, d_2)}{\pi R_{\Delta M}^2}\,. \tag{5.63}$$

Whenever the full disk of the subclump is entirely within the image aperture, the a_2 and a_0 integrals reduce to to the point mass case. However, if the subclump disk overlaps the aperture edge, so that only part of the subclump is within the aperture, then the contribution to both a_2 and a_0 is reduced. We calculate P_2/P_0 as a function of the subclump to cluster distance for individual mergers, and maximize this function. We then use this value for the peak P_2/P_0, instead of equation 5.50, in computing the model ensemble averages (equation 5.53).

The effect of using a finite disk model for the subclump, as opposed to a point mass, is to reduce the power ratio P_2/P_0. Both a_2 and a_0 decrease as the radius of the fixed mass (or fixed luminosity) subclump increases, since less of the subclump will fall within the image aperture. But as the subclump size increases, the distance from the image center for which P_2/P_0 is maximum decreases. The next effect is to decrease P_2/P_0 with increasing subclump radius. Since SCDM clusters and subclumps are more massive than in the low density models, their larger radii $R_{\Delta M}$ lead to even smaller power ratios than those predicted by the point mass model and listed in table 5.2.

As a next level of refinement of our model, we apply the findings of Navarro, Frenk & White (1996), who find evidence in N-body dark matter halos of a universal density profile. This profile,

$$\frac{\rho(r)}{\rho_{crit}} = \frac{\delta_{core}}{(r/r_s)(1 + r/r_s)^2}\,, \tag{5.64}$$

Model	c	$\log(P_2/P_0)_{\text{ensemble}}$
SCDM	7.61	-5.79
OCDM	5.87	-5.64
LCDM	5.04	-5.77

Table 5.3: Predicted ensemble averages of P_2/P_0, based on uniform disk model rather than point mass model.

is universal in the scaled coordinates r/r_s and ρ/ρ_{crit}. The scale radius $r_s = R_{\Delta M}/c$, where the concentration c is related to the core density δ_{core} by

$$\delta_{core} = \frac{200}{3} \frac{c^3}{[\ln(1+c) - c/(1+c)]} . \tag{5.65}$$

The cosmological dependence arises through the concentration factor c, which is sensitive to the mean density at a suitably defined formation time for the halo. The details of this dependence are described in Navarro et al (1996). These authors also made available a FORTRAN subroutine which computes c for a given mass halo in a given cosmological model.

Utilizing this code, we determined the concentration factor appropriate for a cluster of mass M_{low} in each of our models. Table 5.3 lists these concentration factors, as well as the ensemble average P_2/P_0, based on modelling the infalling subclumps as constant surface density disks of radius $R_{\Delta M}/c$. Again, we see that the predicted power ratios do not discrmininate between cosmological models. Here the power ratio predictions are higher than for the point mass model due to the new calibration of P_2/P_0 (using the same calibration event as before). For the SCDM clusters, $R_{\Delta M}$ is larger, but the concentration c is also larger. The competing effects largely cancel, resulting again in a power ratio prediction which is not higher for SCDM than for the low density models.

A more realistic model for the subclump and cluster halos, assuming temporarily that we restrict ourselves to cylindrically symmetric models, will lie somewhere between the extremes of the point mass model and the uniform surface density model, and does not seem to hold any promise for explaining our difference with Buote &

Xu on the SCDM power ratios.

However, one effect which our model in its present form neglects entirely is the possible ellipticity of the cluster and subclump. Buote & Tsai (1995) compute power ratios for spherical and elliptical isothermal β model clusters and find that P_2/P_0 has a strong ellipticity dependence. Table 1 of their paper shows $\log(P_2/P_0)$ for single elliptical clusters varying from 0 at $\epsilon = 0$ to -5.40 at $\epsilon = 0.3$ to -4.79 at $\epsilon = 0.6$, where ϵ is the model cluster's (constant) ellipticity.

If cluster ellipticity is sensitive to cosmology, then adding such a cosmology dependent ellipticity to our model's clusters may lead to higher power ratio predictions for SCDM. We have some indication that this is the case from work by Splinter et al. (1996), who find that "mean ellipticity increases strongly with increasing n" in their studies of N-body clusters. Specifically, they find that ellipticity has no Ω dependence at fixed n, and a strong dependence on n at fixed Ω. They argue that previous authors, particularly de Theije, et al (1995), who claim to have found an Ω dependence were misled when they varied Ω and n simultaneously, as with a CDM type spectrum.

Figure A-21 shows the power spectra for the SCDM, OCDM and LCDM models, along with marks indicating the scale on which the relevant effective slope $n_{\rm eff} = d\ln P/d\ln k$ should be measured. The effective slope for clusters of mass $M_{\rm low}$ is about zero for the SCDM model, and is about $-1/2$ for the other two models. According to the results of Splinter et al (1996), this means the mean cluster ellipticities will be higher for the SCDM model. According to Buote & Tsai (1995), these higher ellipticities will produce higher power ratios.

Clearly the issue of ellipticity as related to power ratios must be considered in future theoretical work. Adding mean cluster ellipticities to our model is a logical next step. At this point, though, we can conclude that any cosmological signal present in the mean power ratios is likely due to the cosmological signal present in the shapes of individual clusters (Splinter et al. 1996, Crone et al. 1994, Navarro et al. 1996a,b). Our model, which takes into account possible cosmological signal in the interaction between cluster and subclump, finds no such signal. We conclude that merger rates, as probed by the power ratios, are not an effective tool for constraining cosmological

parameters.

Our model, based on various oversimplifications such as spherical collapse and two body orbits, and with only one free parameter to normalize the predictions, is not sophisticated enough to predict the power ratio substructure statistic found for simulated clusters. However, it has the convenient feature of being composed of separable parts which can be studied and improved individually. The Press & Schechter formalism, which gives us the mass function and merger rate, has already been a subject of considerable study. The infall model is very simple, with much room for added sophistication, and can be studied as a small problem and improved in its own right. The estimate of the power ratio P_2/P_0 for individual merger events can also be improved by better modelling of the halos. This modelling should include cluster ellipticity, which may have a stronger effect on the ensemble mean P_2/P_0 than do mergers.

We find no cosmological signature in the power ratios which can be traced to halo interactions, and no likely explanation for the lack of such a signal. Any signal which is present is likely due not to interactions, but to the cosmological dependence of individual cluster density profiles.

Chapter 6

Conclusions

We have developed a hybrid N-body/gas code based on the P^3M^2 code of Bertschinger & Gelb (1991) and the KRONOS code of Bryan et al. (1995). This code uses the Piecewise Parabolic Method (Collella & Woodward 1984) to solve Euler's equations for the gas on a grid within a cosmological volume, and a nested variant of the Particle-Particle–Particle-Mesh algorithm (Hockney & Eastwood 1981) to evolve the gravity field and to integrate the trajectories of dark matter particles in an optionally larger volume. The advantage of this approach is that fast methods are used to evolve the gravity field in a large cosmological volume, while the gas dynamics can be solved at high resolution only in a region of interest. This code has been implemented on serial, shared memory parallel, and distributed memory parallel computers, and used to study the formation of an X-ray emitting galaxy cluster.

Such a cluster can be expected to have an equilibrium configuration which is roughly spherical, with density, temperature and luminosity centrally peaked. Whether or not clusters have time to reach equilibrium between mergers is an important observational question. The presence of substructure in a cluster is a signature of recent merger activity. The prevalence of substructure in a fair sample of clusters is an indication of the current merger frequency, which in turn is a probe of the mean mass density Ω as well as other cosmological model parameters.

We have chosen a statistic for measuring substructure in clusters which is well suited to application to our simulated cluster. Cluster simulations are least reliable

in the cluster cores, where high resolution and the physics of gas cooling are required. The power ratio substructure statistic is more sensitive to substructure on the scale of the observing aperture than in the core. We measure the power ratios of the evolving cluster and interpret the trajectories in power ratio space in terms of the progression of merger events. We determine that power ratios sourced by the X-ray surface brightness are biased low with respect to those sourced by the square of the gas density, which in turn is biased low with respect to those sourced by the square of the dark matter density. The latter bias is present in the results of Buote & Xu (1996), but the effect is small.

Observation of merging events in this simulation (and others) reveal that most mergers occur along radial orbits. This fact leads us to propose a simple model for the mergers between clusters and subclumps. This model combines the seemingly contradictory ideas of spherical collapse and two body orbits. The spherical collapse model has been shown, in the contexts tested, to reproduce well the merger rate observed in simulations. However, it is clear from studying any hierarchical clustering simulation that halo collapse and formation is anything but spherical. While some continuous, roughly spherical accretion may occur on a cluster, the main contribution to its increasing mass is due to mergers with significant subclumps. Thus, while the spherical collapse model may predict the merger rate, a two body orbit resembles more closely what actually occurs in a merger.

Combining the merger rate derived from spherical collapse with the infall model derived from the two body orbit, and adding an estimate of the peak of the power ratio P_2/P_0 as a function of the merging masses, we derive an expression for the average, over an ensemble of rich clusters, of the logarithm of the mean P_2/P_0. This expression reproduces reasonably well the mean P_2/P_0 obtained by Buote & Xu (1996) for their simulations of low density CDM models, but fails in the case of high density "Standard" CDM.

We investigate possible sources for this discrepancy, and find none related to the interactions between the cluster and subclumps falling onto it. We argue that the likely cause of the discrepancy is our model's lack of consideration of cluster ellipticity.

Although it is presently simple and inaccurate in detail, our analytic power ratio model holds some promise as a tool for studying the cosmological signatures in galaxy cluster structures. The model elements are separable and can be tested and improved individually. The one free parameter in the model was set by considering separate parts of the model, the merger infall time $t_{\rm fall}$ and the peak of the power ratio P_2/P_0 for a merger between components of given masses. Still, the combined model did produce predictions that were in good agreement with N-body reults for the low density cosmological models. And further improvement is to be expected. The infall model can be improved by studying merger events in large N-body simulations. Significantly less than the state of the art in computers and simulation methods is required here, as very large particle numbers and fine force resolution are not required. These features are necessary when internal features of dark matter halos, such as core radii, are studied. They are not necessary when only the first interaction of a merging pair is required. Finally, the power ratio prediction can be improved by replacing the uniform spheres or point masses in the model with realistic halo profiles, using, for example, the "universal" halo profile presented by Navarro et al. (1995, 1996). These are all tasks for the near future.

However, if cluster ellipticity plays a significant role in the power ratios, as we argue above, then the relationship between mergers and power ratios may be cosmologically irrelevant. In that case, the high power ratio events corresponding to mergers are not cosmologically sensitive, while the lower power ratios corresponding to unperturbed elliptical halos are. This would seem to suggest using power ratios or some other measure of cluster ellipticity as a cosmological probe. This seems difficult, however, as the range of effective power spectral slopes, on cluster scales, for different models, is small. In addition, observational uncertainty in the cluster mass translates to uncertainty in the scale at which the spectral slope is being probed. Even a successful measurement of the spectral slope on cluster scales adds only one data point to our knowledge of the initial power spectrum, at a time when other methods, such as CMB anisotropy measurements, promise more.

Our results are specific to X-ray observations and power ratios. The question of

cosmological signatures in optical cluster data is still an open question. Nevertheless, we agree with the conclusion of Splinter et al. (1996) that cluster morphology is a less powerful probe of cosmology than has been hoped.

Appendix A

Computational details

Here are described many of the supplemental codes used, as well as the many detailed changes to the main P8M3 code.

A.1 Initial Conditions

Before the P8M3 code can be run initial conditions must first be generated. For this purpose I used the COSMICS package of Bertschinger (1995). COSMICS uses separate codes for generating the power spectrum of initial density perturbations and for generating particular realizations. This second code, GRAFIC, produces initial displacements and velocities for dark matter particles whose positions at infinite redshift are on a uniform three dimensional grid. As I required 100 kpc resolution in the center of a 51.2 Mpc volume, it was necessary to produce full initial conditions on a 512^3 grid. As originally written, GRAFIC requires storage for 12.5 grids of this size; six for displacement and its Fourier transform, three for velocity, two for density and its Fourier transform, one for the constraint matrix, and and one half for the power in each mode [1]. This gives a total memory requirement of 6.7 Gigabytes! Much of this memory usage is unnecessary and was included originally for simplicity and slight speed advantages, and was easily eliminated. Four grids were removed by

[1] The array containing the power in each Fourier mode is real, and hence requires half the storage of the complex Fourier space arrays

storing the complex Fourier transform arrays in the same space as the corresponding real arrays. The three displacement grids were also removed, as they can be easily computed later from the velocity field. Further memory savings were bought at the expense of CPU time by running the modified GRAFIC code four times, once for the density and each of the three coordinate velocities, for a further reduction in memory of three grids. Rather than running the complete code each time, intermediate results were written on the first run so that the next three could be restarted from that point in the calculation. The half gigabyte of storage for the power array was also saved at CPU expense by calculating the power each of the four times it was needed, rather than saving it.

The only point in the GRAFIC computation where two large grids is required is the convolution of the density field with the constraint field. To save more storage, the constraint field was written to disk and read in small portions as needed. This brought the total storage requirement down to just slightly more than one large grid, or 512 Megabytes. This storage was available on a DEC Alpha workstation, although most of it was in the paging space. Here we encountered another roadblock when the GRAFIC code attempted to perform the Fast Fourier Transform (FFT). The transform on the third dimension requires striding through the 512^3 array in steps of 512^2, resulting in the machine spending all its time paging data. This problem was addressed by writing a transpose operation to transpose the first and third dimensions. This transpose was performed on one 128^3 block of the large three dimensional array at a time, so that the supplemental memory required was only an extra 1.5%.

The result of all these manipulations was to produce 512^3 grids of density and velocity. Each of the velocity fields was converted to position via the Zel'dovich approximation by a separate code.

This is much more data than necessary for a simulation of a single cluster. The high resolution is only needed in the center of the volume, where the cluster will form. Far from the cluster the mass field can be represented by fewer, more massive particles. To complete the preparation of the particle initial conditions, particles far from the center of the simulation volume are combined. Specifically, the initial

particle spacing in the central 13 Mpc cube is 100 kpc, yielding particles of masses of $4.7 \times 10^7 M_\odot$. The surrounding 4 Mpc has twice the particle spacing and eight times the mass. Two more layers of 6.4 and 7.2 Mpc each have double the spacing and eight times the mass of the previous layer. These heavy particles represent the large scale mass distribution far from the developing cluster. The result is a total of just over six million dark matter particles.

The central 100^3 points in the 512^3 initial conditions are used to generate the initial conditions for the gas. The gas density is set proportional to the total density, the gas velocity is set equal to the particle velocity, and these are read by the KRONOS portion of the P8M3 code, which sets the gas temperature assuming spatially constant entropy and a mean gas temperature appropriate to the initial redshift.

A.2 P8M3

Constructing the P8M3 code from P3M2 and KRONOS required the conceptual changes described in chapter 2 as well as other modifications made for the sake of efficiency. Those changes made to the message passing version of the code are described here.

Due to the highly clustered nature of the problem, even initially, it was apparent immediately that the gravity code efficiency could be increased by increasing the size of the PM grid, thus reducing the amount of work performed by PP and the adaptive fine grids. Because the PM calculation is the most memory intensive portion of the code, certain modifications were made to minimize memory usage. The real and Fourier space density and force arrays, originally stored separately, were combined. Since each component of the force array is the convolution of the density with a Green's function, density and force are usually stored separately. One code modification was to have the code attempt to allocate separate storage for these two large arrays. If the requisite storage was unavailable, these were combined by storing the Fourier transformed density on disk during the force calculations. The time required for this disk I/O was no more than a few percent of the computation time.

Another memory savings was achieved in the FFT routine. Because the spatial volume of the simulation was partitioned among processors as slabs in the z coordinate direction, the FFT along the x and y dimensions could be performed independently on each processor. The z dimension FFT was enabled by first transposing the y and z dimensions. As originally written the transpose was capable of handling rectangular non-cubic grids. The price of this generality was that a temporary array equal in size to the full array had to be allocated to receive the transposed array sections from the other processors. By accepting the restriction that the y and z coordinate axes were the same length I wrote another transpose which performed paired send and receive operations between pairs of processors. The temporary storage required was only as large as the largest of these chunks, which was less than one tenth of the previous temporary storage requirement.

Even with these memory savings allowing for the largest possible PM grid, the computation was still dominated by the short range force correction. The primary cost of the fine mesh PM is in the FFTs, and hence is fixed for each chaining mesh cell. For sufficiently densely populated cells, the sub-PP computation dominates the fine mesh PM. Hence, an added level of fine mesh was added to the code. Thus, if a cell is sparsely populated the short range force correction will be performed by the PP subroutine. Cells above a given threshold in number density (here, 1500) are handled by a fine mesh PM grid of size 48^3, followed by sub-PP. A second, higher threshold (here, 3000) determines which cells use a 96^3 fine mesh grid.

Computational load balancing is also affected by the high degree of clustering in the simulation. The P3M2 code load balances the calculation by adjusting the widths in the z direction of the slabs assigned to each processor, based on the time spent in computation on the processor. Because the clustering is strong, the PP and adaptive mesh portions of the gravity code dominate the CPU time. In the center of the volume where most of the dark particles and all of the gas reside, this load balancing scheme shrinks domains, enlarging those domains far from the cluster. However there is a minimum limit on the width of a domain imposed by the width of the cells used by the PP calculation. This limit is three PM grid spacings. There

is also an upper limit imposed by memory constraints. As the clustering increases during the simulation, this load balancing scheme begins to break down when these limits are enforced. Then the narrow domains in the center of the volume take more time than the wider domains, but cannot shrink further due to the minimum width limit. The wider domains sit idle while the narrow domains compute pair forces in PP. Due to the communication in the transpose, the processors are synchronized in the PM routine, but are unsynchronized through the adaptive mesh and PP routines. The effect of the load imbalance is that some processors finish PP before others.

Two code modifications were made to alleviate this problem. First, the restriction on the minimum domain width was removed. The restriction existed so that each domain would need to communicate with only its next door neighbor in order to locate the particles for which the short range force correction was required. Removing the restriction involved providing for each processor to be able to communicate with processors which are 3 domains away.

The second modification to remedy this problem was to develop a finer level of load balancing. When a processor finishes with the short range force corrections (PP and fine mesh PM) on its own particles, it sends a message to all others offering help. Those processors which have yet to finish their short range force calculations check for such messages as they loop over chaining mesh cells [2]. Estimating the work required for each chaining mesh cell by the product of the number of particles in the cell and the number of particles in neighbor cells, this processor checks for messages offering help whenever the time required to do the work is great enough to justify the communication expense of sending it to another processor. When a message offering help is received, the receiving process replies in order to establish a commitment by the offering process. This handshaking is required to ensure that more than one process at a time does not accept help from the same offering processor. Then the processor requesting help sends the appropriate data (the number of particles in the

[2]The neighbor search required for the pair force calculation is facilitated by dividing the domain into chaining mesh cells, each 2.78 PM grid spacings in width. The short range force subroutine loops over chaining mesh cells, searching the central cell and its neighbors for near particle pairs.

central chaining mesh cell, the number in the central and neighbor cells, particle lists of position, mass, and particle index) to the helping processor, which computes the pair forces. Meanwhile the processor which requested the help continues to the next chaining mesh cell, periodically checking to see if the results have been returned. Each processor knows that all processors are finished when it has received an offer of help from each. Of course, if no offer of help message has been posted when a processor checks for it, that processor must perform the work itself.

This added level of load balancing worked well, until the simulation reached a new bottleneck due to even stronger clustering. The clustering became so strong that the short range force calculation for one the few chaining mesh cells at the cluster's center took half or more of the total short range force calculation time. This left one unlucky processor working on the cluster center all by itself even after other processors were finished. The remedy for this problem was to loop over the chaining mesh cells not in the naive order, but instead in decreasing order of the amount of work, estimated by the number of particles in the cell. Then a a "high priority" request for help message was added to the scheme described above. Due to the new ordering of chaining mesh cells, the densest are tackled first. If a cell is extremely densely populated, the processor which owns it send a "high priority" request for help, then waits whether an offer of help is present or not. Because the processors whose domains are far from the cluster are lightly loaded, they finish their own work in a few seconds, and then accept the "high priority" work from the cluster center. This ensures that the processor whose domain includes the cluster center is able to farm out a significant fraction of its workload right away.

As before, this improvement was sufficient until the clustering progressed even further, to the point that a single, extremely dense chaining mesh cell would require more CPU time to perform the sub-PP computation than would all the other chaining mesh cells in that domain combined. Even with the "high priority" help described above ensuring that this cell's short range force calculation was farmed out to a lightly loaded processor, this situation resulted in processors sitting idle while the single most dense chaining mesh cell was still being handled. The remedy was a third level of

fine mesh refinement. Chaining mesh cells populated with more than 30000 particles used a fine mesh PM grid of size 192^3, followed by sub-PP.

In order to generate the Green's function required for the fine meshes, an FFT three times larger in each dimension must be performed. This extra size is the buffering required to generate an anti-aliasing Green's function appropriate for the isolated (non-periodic) boundary conditions on the chaining mesh cell (see Hockney & Eastwood, 1981). For the two smaller fine mesh sizes (48^3 and 96^3), the memory and CPU cost of computing the Green's function is sufficiently small that each processor performs the calculation. However, the memory requirement for generating the largest fine mesh Green's function $((192 * 3)^3$ is about 750 Mbytes, well beyond the amount available on most processors of the IBM SP2 on which the simulation was performed. Therefore this Green's function was generated separately on an SP2 node with 1024 Mbytes of memory and stored. This Green's function was read from disk as needed by the processors during the simulation.

Bibliography

[1] Abell, G. O. 1958, ApJ Suppl, 3, 211

[2] Abell, G. O. 1965, ARA&A, 3, 1

[3] Abell, G. O. 1975, in Stars and Stellar Systems IX: Galaxies and the Universe, eds Sandage, A., Sandage, M., & Kristian, J., 601. Chicago: University of Chicago

[4] Bardeen, J. M., Bond, J. R., Kaiser, N., & Szalay, A. S. 1986, ApJ, 304, 15

[5] Bautz, L. P., & Morgan, W. W. 1970, ApJL, 162, L149

[6] Bertschinger, E. 1995, astro-ph/9506070

[7] Bertschinger, E., & Gelb, J. M. 1991, Computers in Physics, 5, 8

[8] Bond, J. R., Cole, S., Efstathiou, G., & Kaiser, N. 1991, ApJ, 379, 440

[9] Bryan, G. L. 1996, Ph.D. Dissertation, University of Illinois

[10] Bryan, G. L., Norman, M. L., Stone, J. M., Cen, R., & Ostriker, J. P. 1995, Comput. Phys. Comm., 89, 149

[11] Buote, D. A., & Tsai, J. C. 1995, ApJ, 452, 522

[12] Buote, D. A., & Tsai, J. C. 1996, ApJ, 458, 27

[13] Buote, D. A., & Xu, G. 1996, astro-ph/9609051

[14] Chandrasekhar, S. 1943, Rev. Mod. Phys., 15, 2; reprinted in Selected Papers on Noise and Stochastic Processes, ed. N. Wax (New York: Dover 1954)

[15] Colella, P. & Woodward, P. R. 1984, J. Comput. Phys., 54, 174

[16] Crone, M. M., Evrard, A. E., & Richstone, D. O. 1994, ApJ, 434, 402

[17] de Theije, P. A. M., Katgert, P., & van Kampen, E. 1995, MNRAS 273, 30

[18] Dressler, A., & Shectman, S. A. 1988, AJ, 95, 985

[19] Efstathiou, G., Frenk, C. S., White, S. D. M., & Davis, M. 1988, MNRAS, 235, 715

[20] Efstathiou, G., & Rees, M. J. 1988, MNRAS, 230, 5p

[21] Evrard, A. E., Mohr, J. J., Fabricant, D. G., & Geller, M. J. 1993, ApJ, 419, L9

[22] Geller, M. J., & Beers, T. C. 1982, PASP, 94, 421

[23] Gnedin, N. Y. 1995, ApJS, 97, 231

[24] Gunn, J. E., & Gott, J. R. 1972, ApJ, 176, 1

[25] Hockney, R. W., & Eastwood, J. W. 1981, Computer Simulation Using Particles, (New York: McGraw-Hill)

[26] Jing, Y. P., Mo, H. J., Boerner, G., & Fang, L. Z. 1995, MNRAS,

[27] Kauffmann, G., & White, S. D. M 1993, MNRAS, 261, 921

[28] Kochanek, C. S. 1996, ApJ, 466, 638

[29] Lacey, C., & Cole, S. 1993, MNRAS, 262, 627

[30] Lacey, C., & Cole, S. 1994, MNRAS, 271, 676

[31] Liddle, A., Lyth, D., Viana, P., & White, M. 1995, astro-ph/9512102

[32] McGlyn, T. A., & Fabian, A. C. 1984, MNRAS, 208, 709

[33] Mohr, J. J., Evrard, A. E., Fabricant, D. G., & Geller, M. J. 1995, ApJ, 447, 8

[34] Mohr, J. J., Fabricant, D. G., & Geller, M. J. 1993, ApJ, 413, 492

[35] Morgan, W. W. 1961

[36] Nakamura, F. E., Hattori, M., & Mineshige, S. 1995, A&A, 302, 659

[37] Navarro, J. F., Frenk, C. S., & White, S. D. M. 1995, MNRAS, 275, 720

[38] Navarro, J. F., Frenk, C. S., & White, S. D. M. 1996, ApJ, 462, 563

[39] Navarro, J. F., Frenk, C. S., & White, S. D. M. 1996, astro-ph/9611107

[40] Oemler, A. Jr. 1974, ApJ, 194, 1

[41] Ostriker, J. P. & Steinhardt, P. J. 1995, Nature, 377, 600

[42] Pen, U. 1995, ApJS, 100, 269

[43] Pfeffermann, E. et al. 1987, Proc. SPIE, 733, 519

[44] Press, W. H., & Schechter, P. L. 1974, ApJ, 187, 245

[45] Press, W. H., Teukolsky, S. A., Vetterling, W. T., & Flannery, B. P. 1992, Numerical Recipes, (Cambridge: Cambridge Univeristy Press)

[46] Richstone, D., Loeb, A., & Turner, E. L. 1992, ApJ, 393, 477

[47] Rood, H. J., & Sastry, G. N. 1971, PASP, 83, 313

[48] Ryu, D., Ostriker, J. P., Kang, H., & Cen, R. 1993, ApJ, 414, 1

[49] Sarazin, C. L. 1988, X-ray Emission from Clusters of Galaxies, (Cambridge: Cambridge University Press)

[50] Splinter, R. J., Melott, A. L., Linn, A. M., Buck, C., & Tinker, J. 1996, ApJ in press, astro-ph/9607144

[51] Tsai, J. C., & Buote, D. A. 1996, MNRAS, in press (astro-ph/9510057)

[52] West, M. J., & Bothun, G. D. 1990, ApJ, 350, 36

[53] White, S. D. M., Efstathiou, G., & Frenk, C. S. 1993, MNRAS, 262, 1023

[54] White, S. D. M., Navarro J., Evrard, A. E., & Frenk, C. S. 1993, Nature, 366, 429-433

[55] Zwicky, F., Herzog, E., Wild, P., Karpowicz, M., & Kowal, C. T. 1961-1968, Catalogues of Galaxies and Clusters of Galaxies, Vol. 1-6. Pasadena: Caltech

Figures

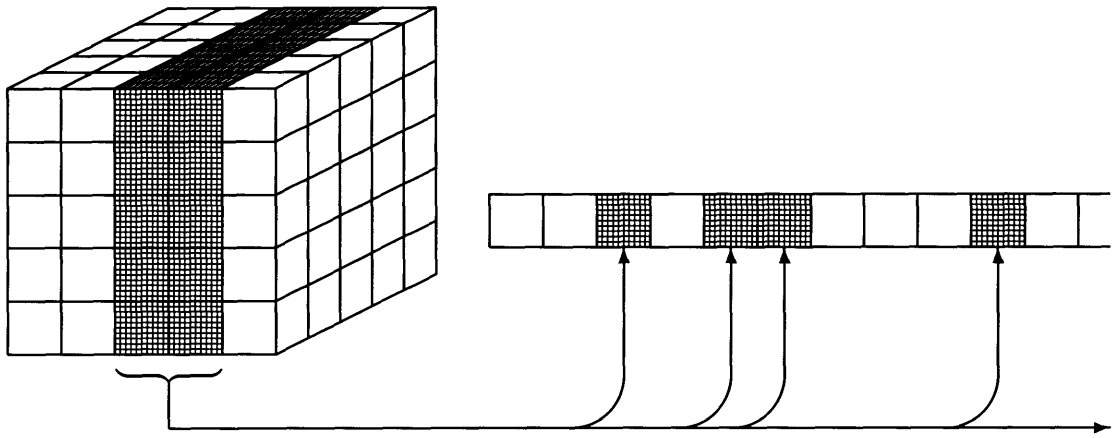

Figure A-1: Data motion from gas grid structure to particle list structure.

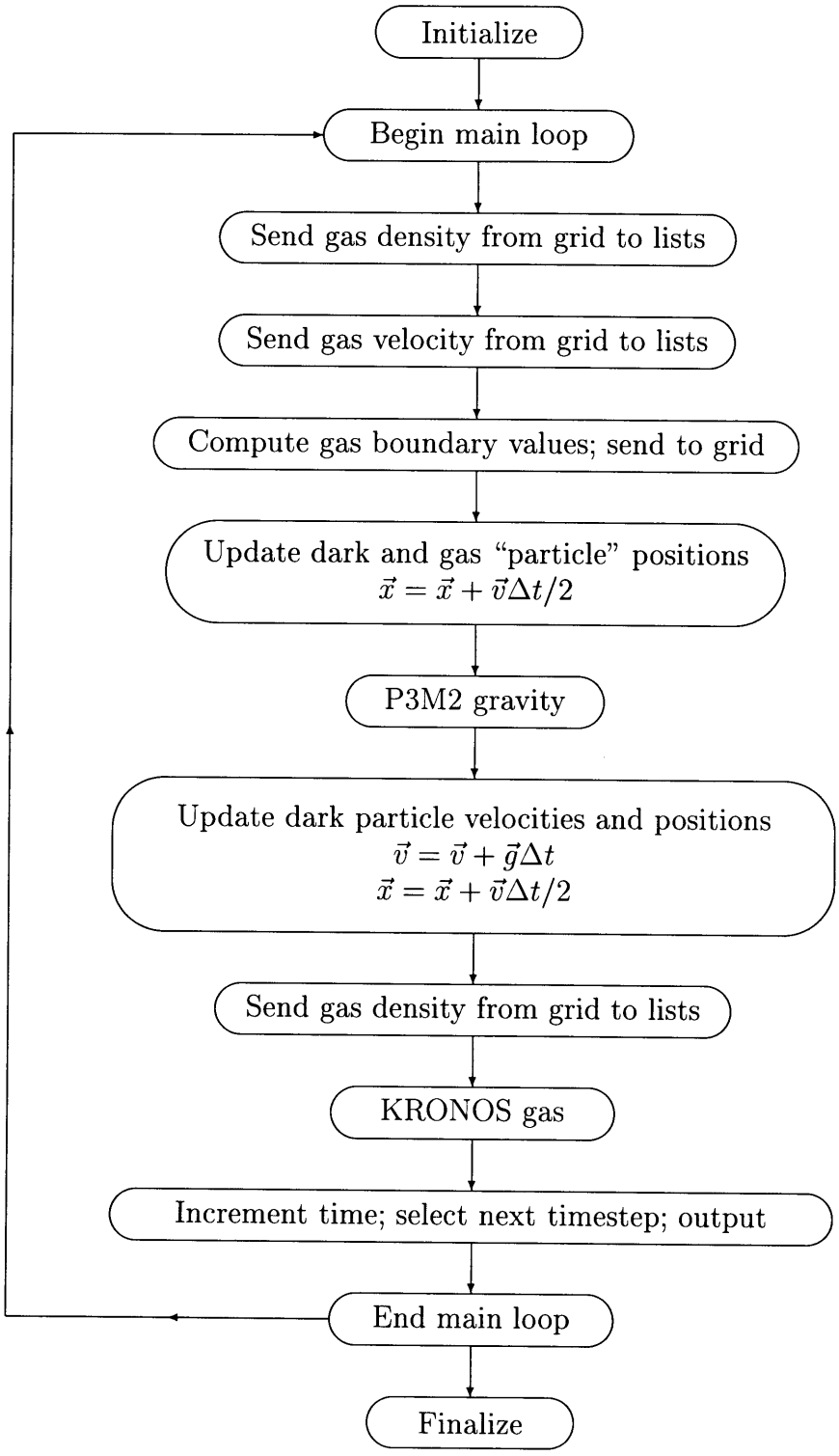

Figure A-2: Basic P8M3 code structure.

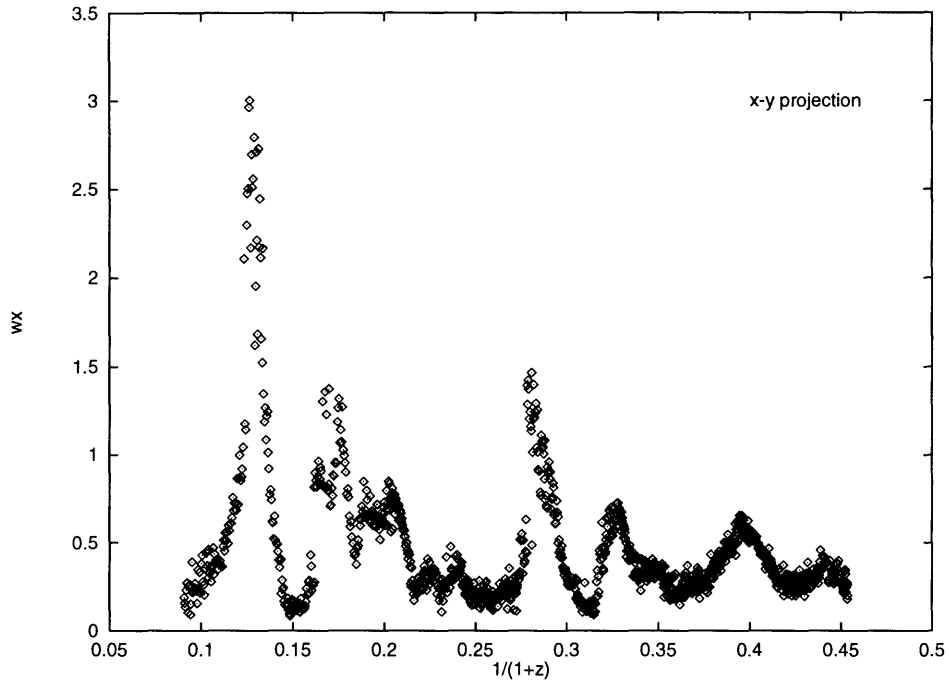

Figure A-3: Emission weighted centroid shift versus expansion factor for the $x - y$ projection of the cluster.

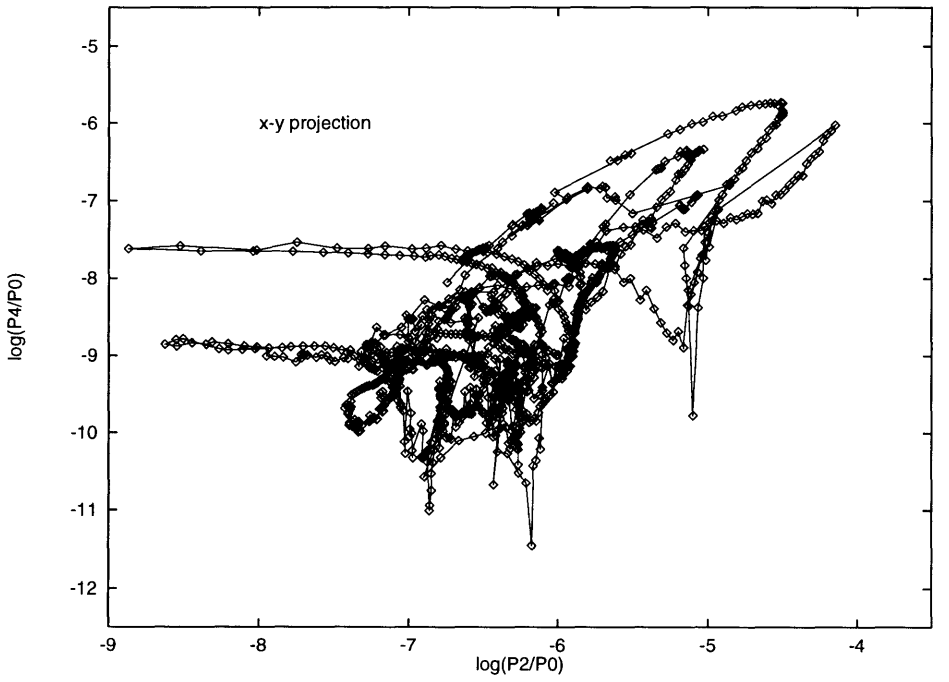

Figure A-4: Trajectory followed by the $x - y$ projection of the cluster in the $P_2/P_0 - P_4/P_0$ plane.

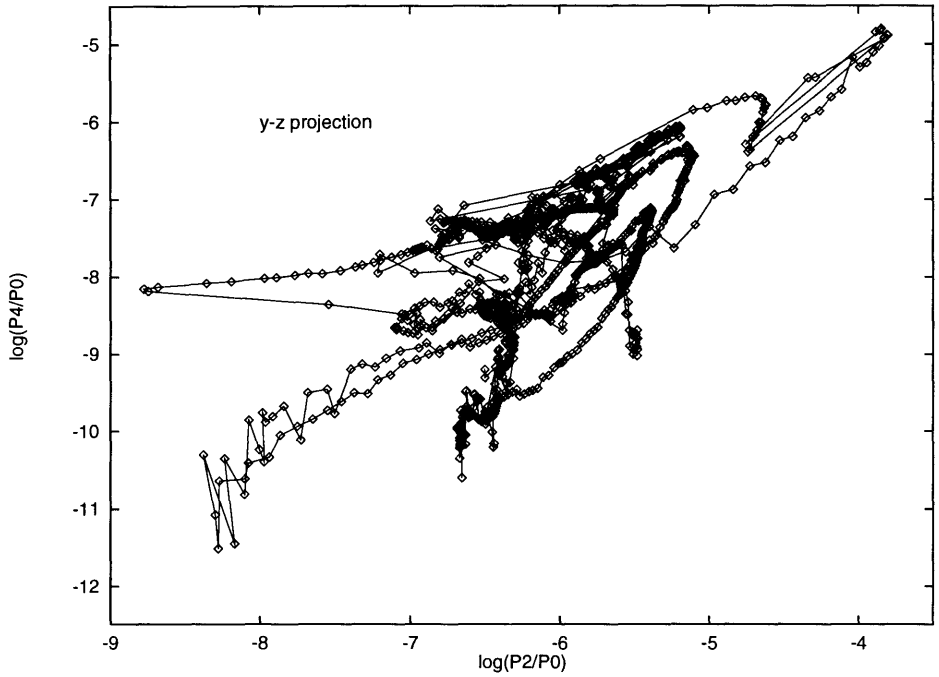

Figure A-5: Trajectory followed by the $y-z$ projection of the cluster in the $P_2/P_0 - P_4/P_0$ plane.

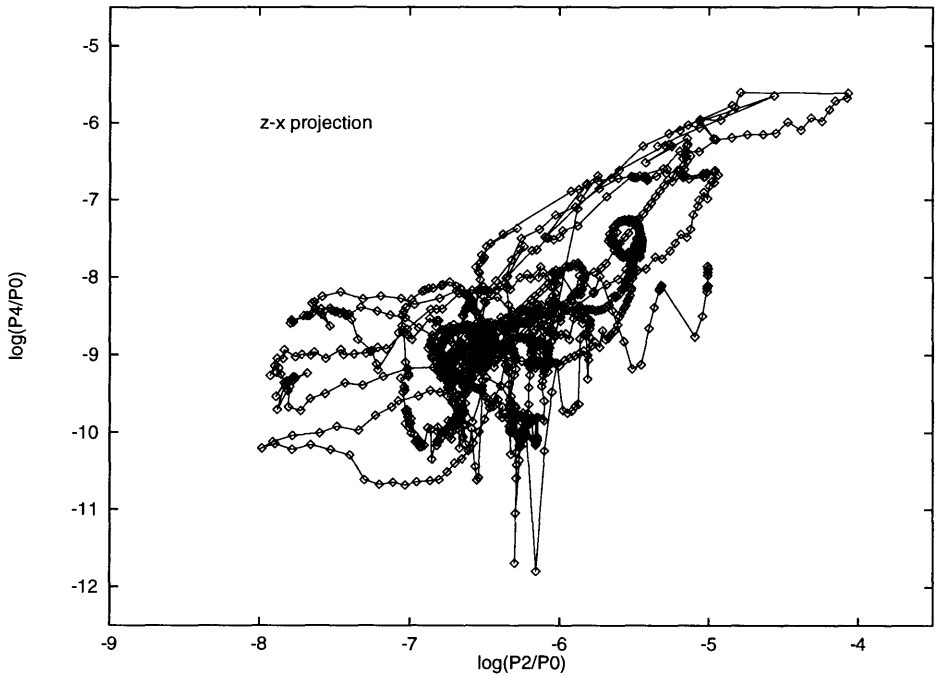

Figure A-6: Trajectory followed by the $z-x$ projection of the cluster in the $P_2/P_0 - P_4/P_0$ plane.

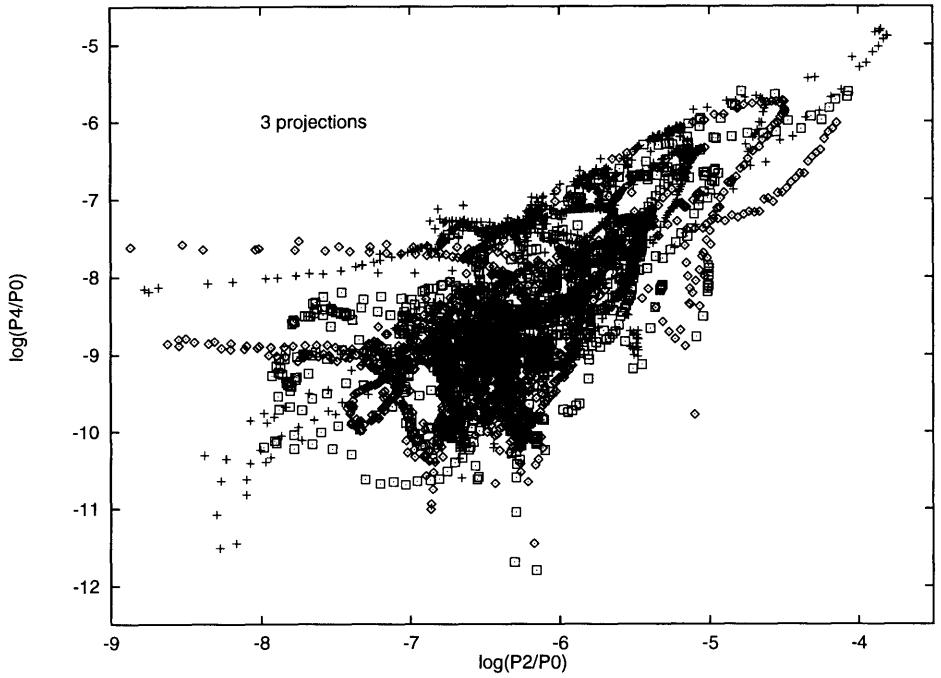

Figure A-7: Combined trajectories for 3 orthogonal projections of the cluster in the $P_2/P_0 - P_4/P_0$ plane.

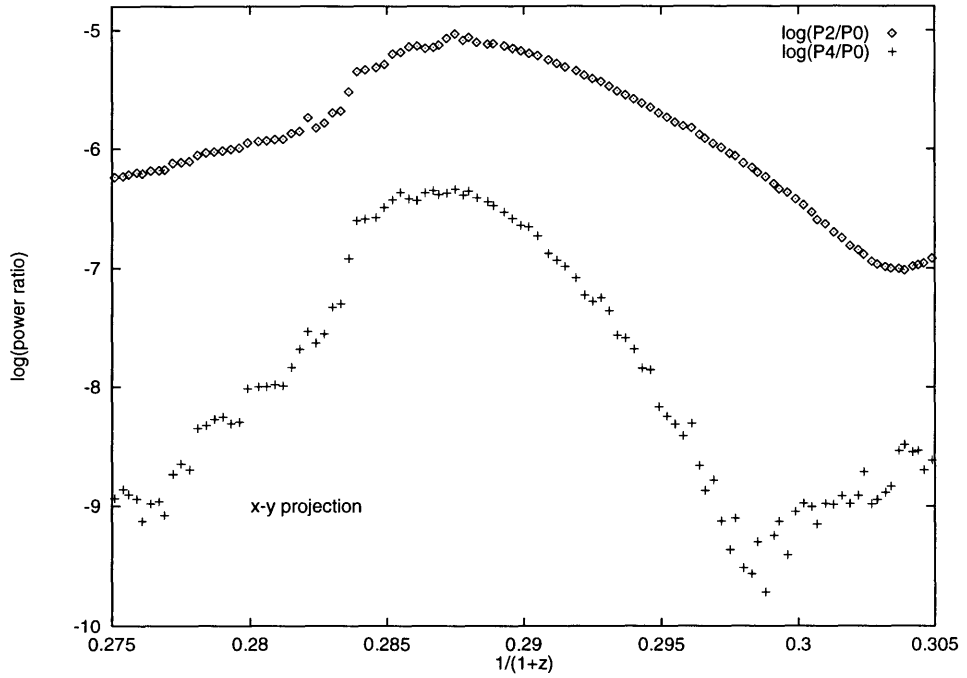

Figure A-8: Power ratios P_2/P_0 (diamonds) and P_4/P_0 (crosses) versus expansion factor for the $x - y$ projection, near the high power excursion at $z \approx 2.5$.

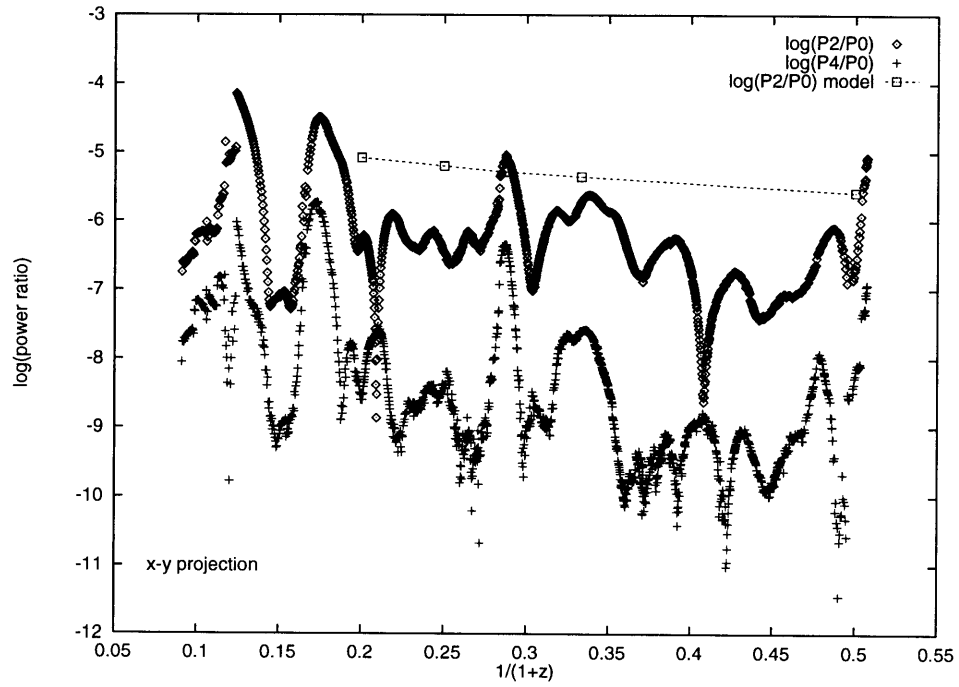

Figure A-9: Power ratios P_2/P_0 (diamonds) and P_4/P_0 (crosses) versus expansion factor for the $x-y$ projection. Also plotted are the predictions of equation 5.51 at redshifts 4, 3, 2.5, 2 and 1, connected by the dotted line.

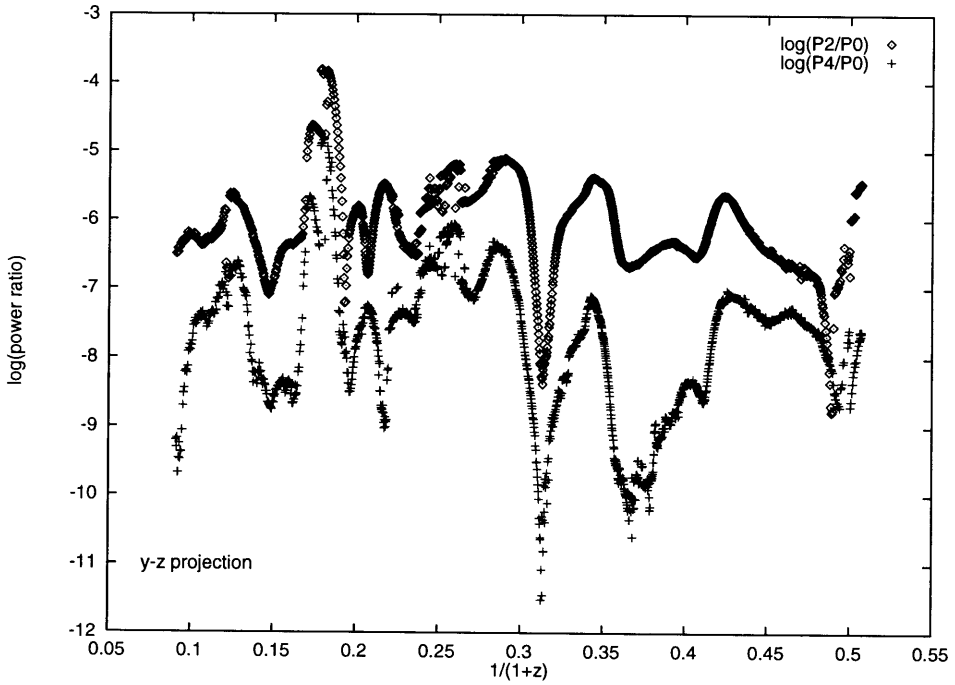

Figure A-10: Power ratios P_2/P_0 (diamonds) and P_4/P_0 (crosses) versus expansion factor for the $y-z$ projection.

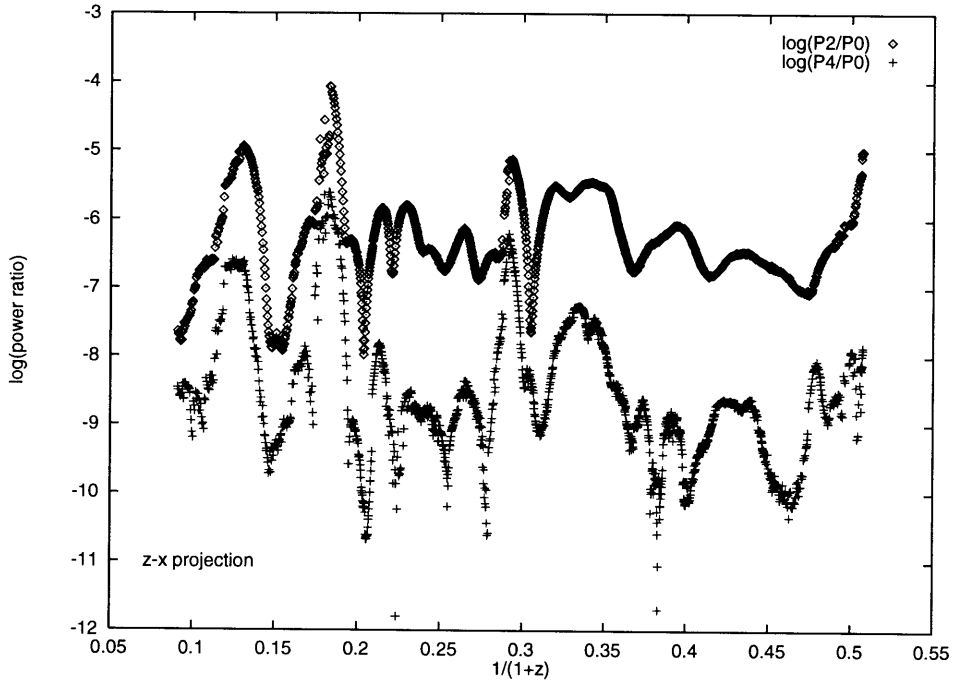

Figure A-11: Power ratios P_2/P_0 (diamonds) and P_4/P_0 (crosses) versus expansion factor for the $z - x$ projection.

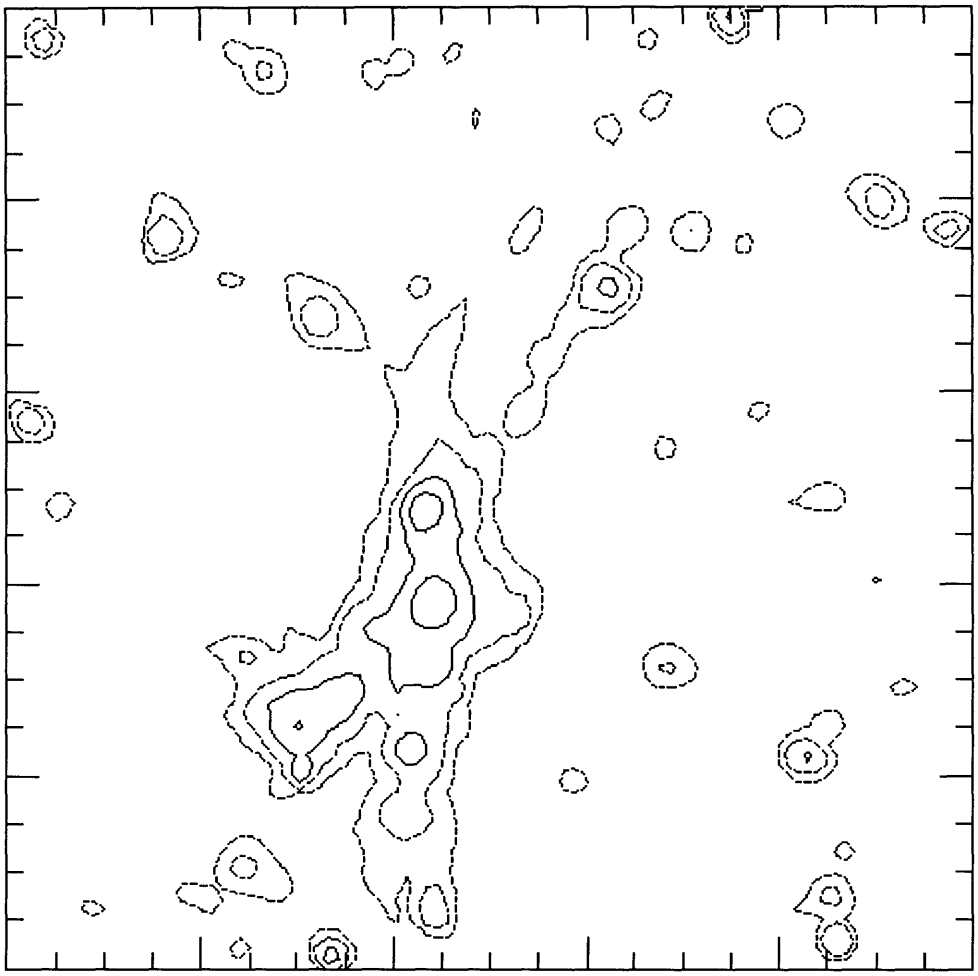

Figure A-12: X-ray contours during a merger sequence. Contours are spaced by factors of ten, with the highest contour at 1/10 the peak value. Each panel is a 10 comoving Mpc square. Sequence proceeds from panel A to panel G, covering a timespan of 0.3 Gyr. This is Panel A.

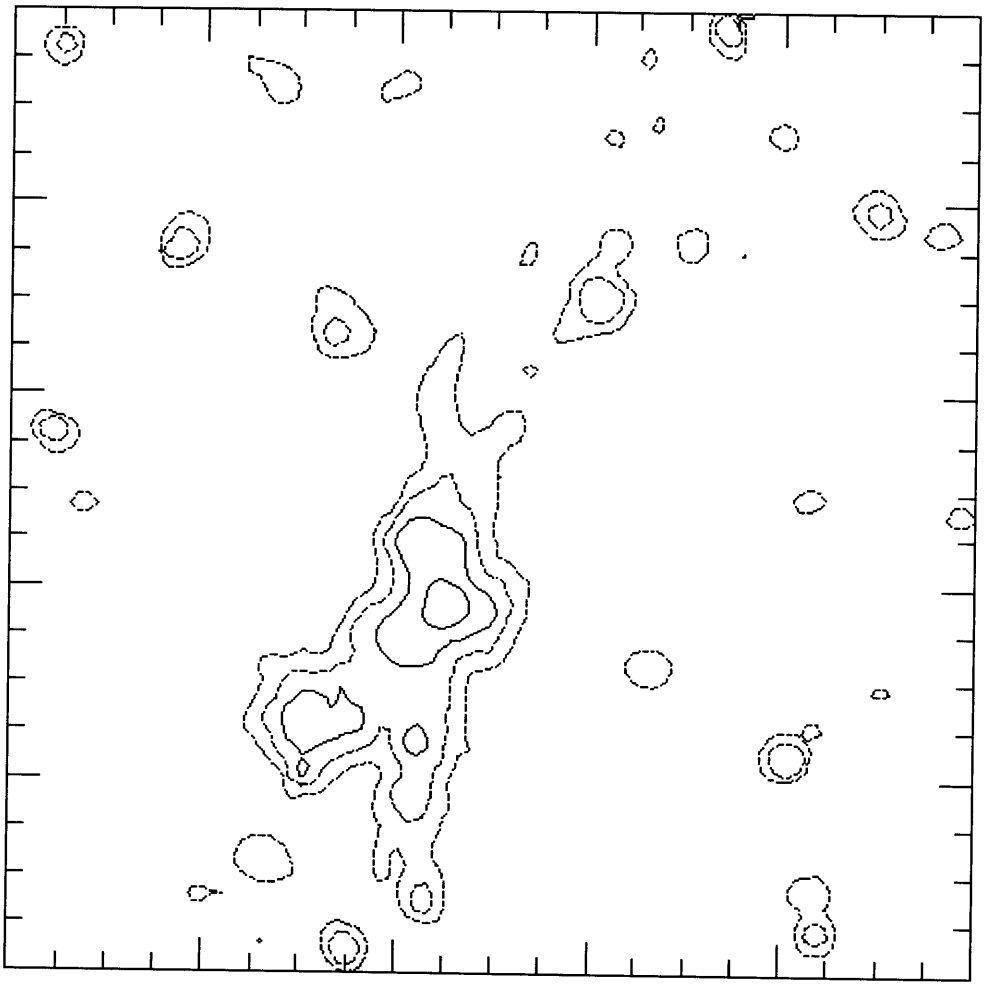

Figure A-12: Panel B.

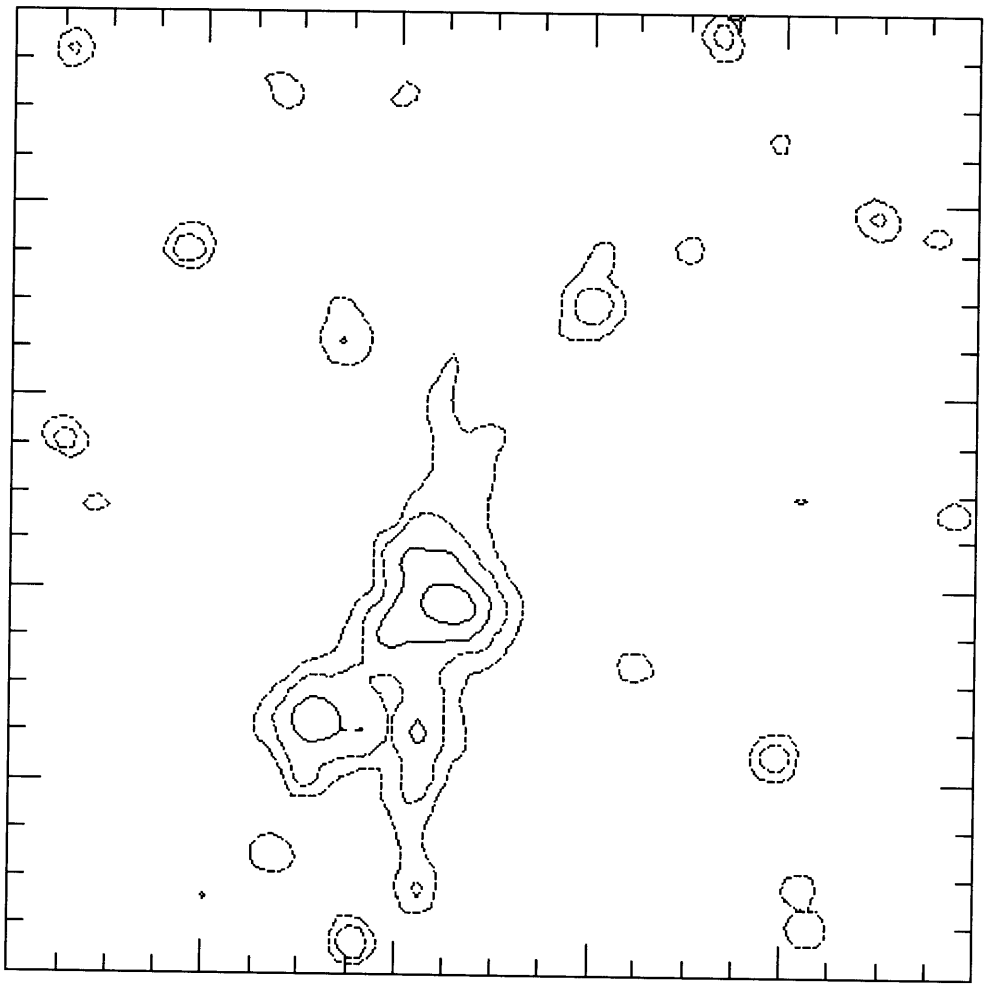

Figure A-12: Panel C.

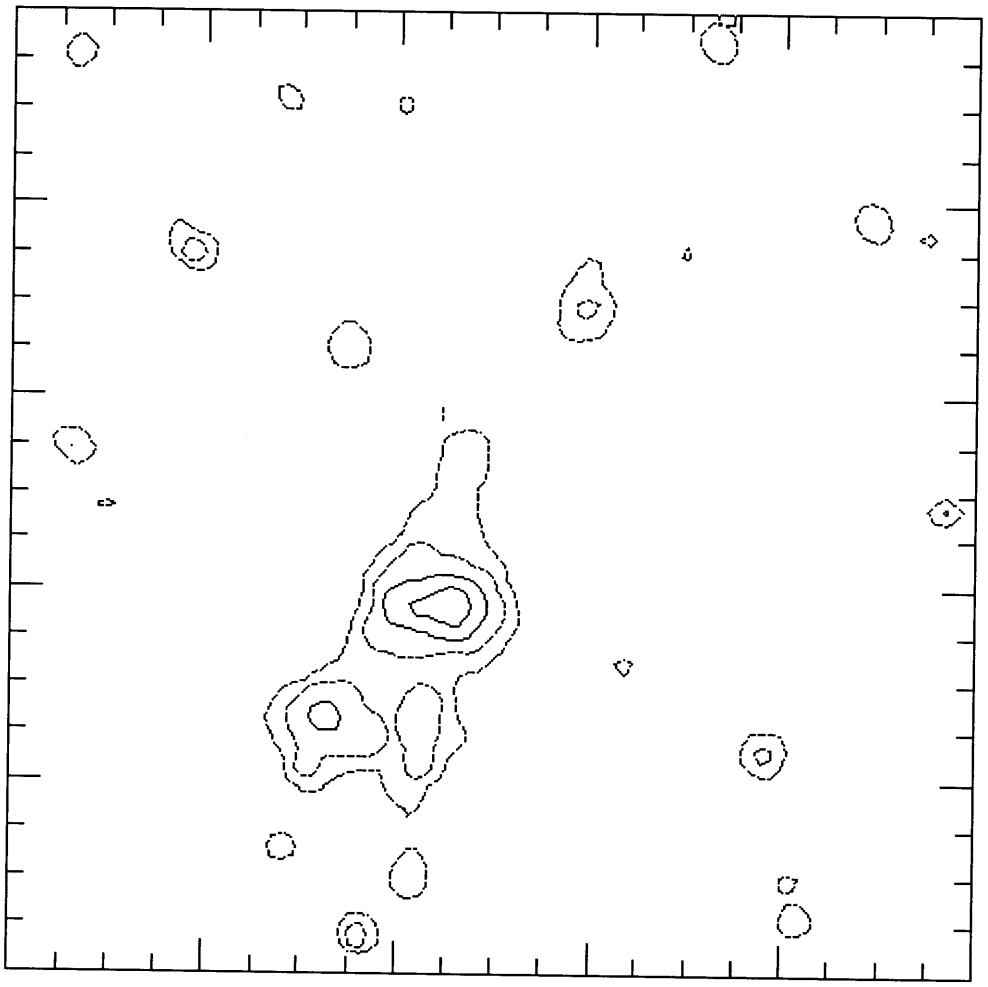

Figure A-12: Panel D.

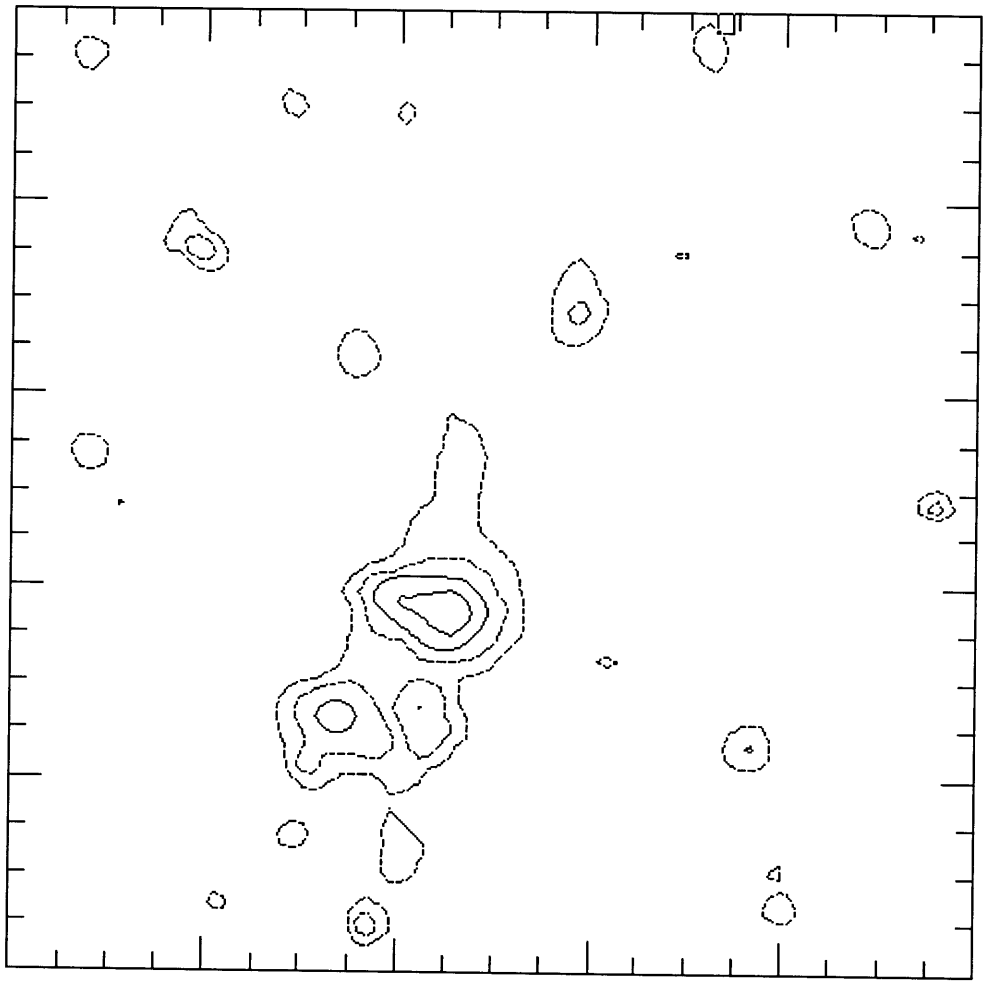

Figure A-12: Panel E.

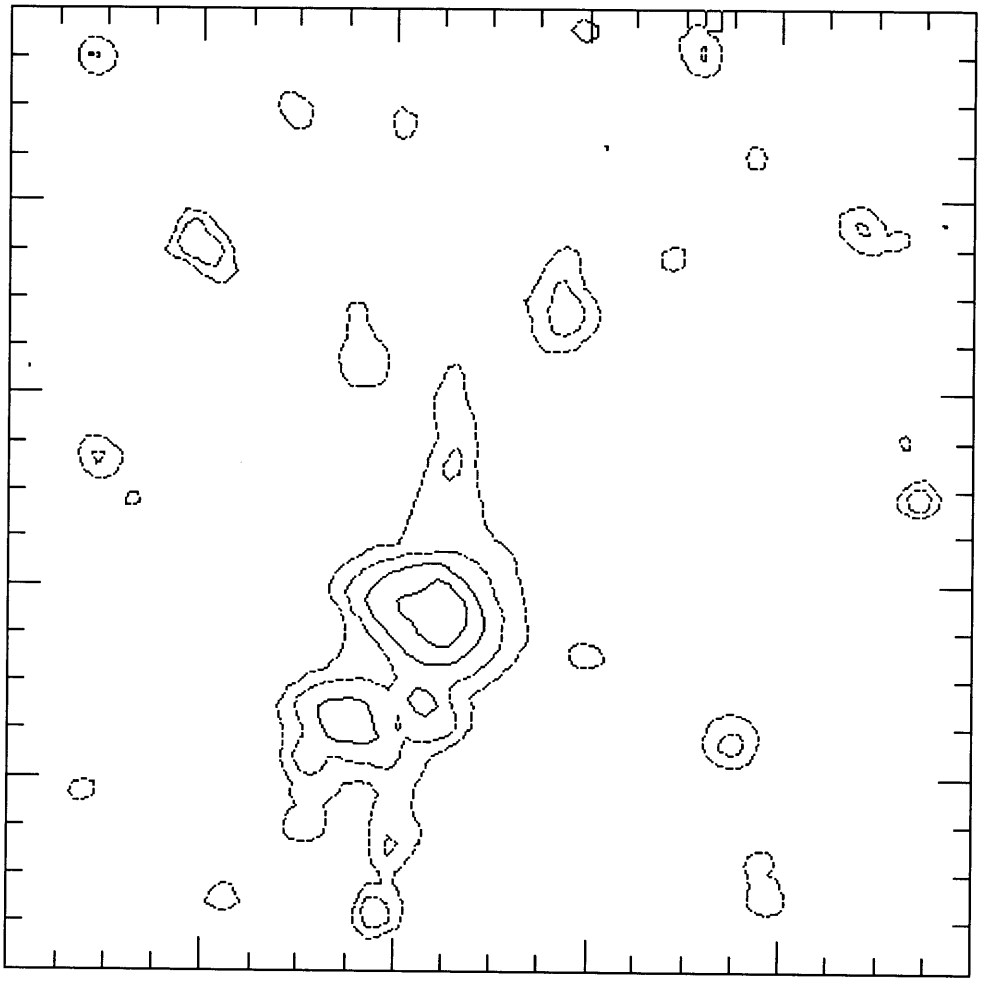

Figure A-12: Panel F.

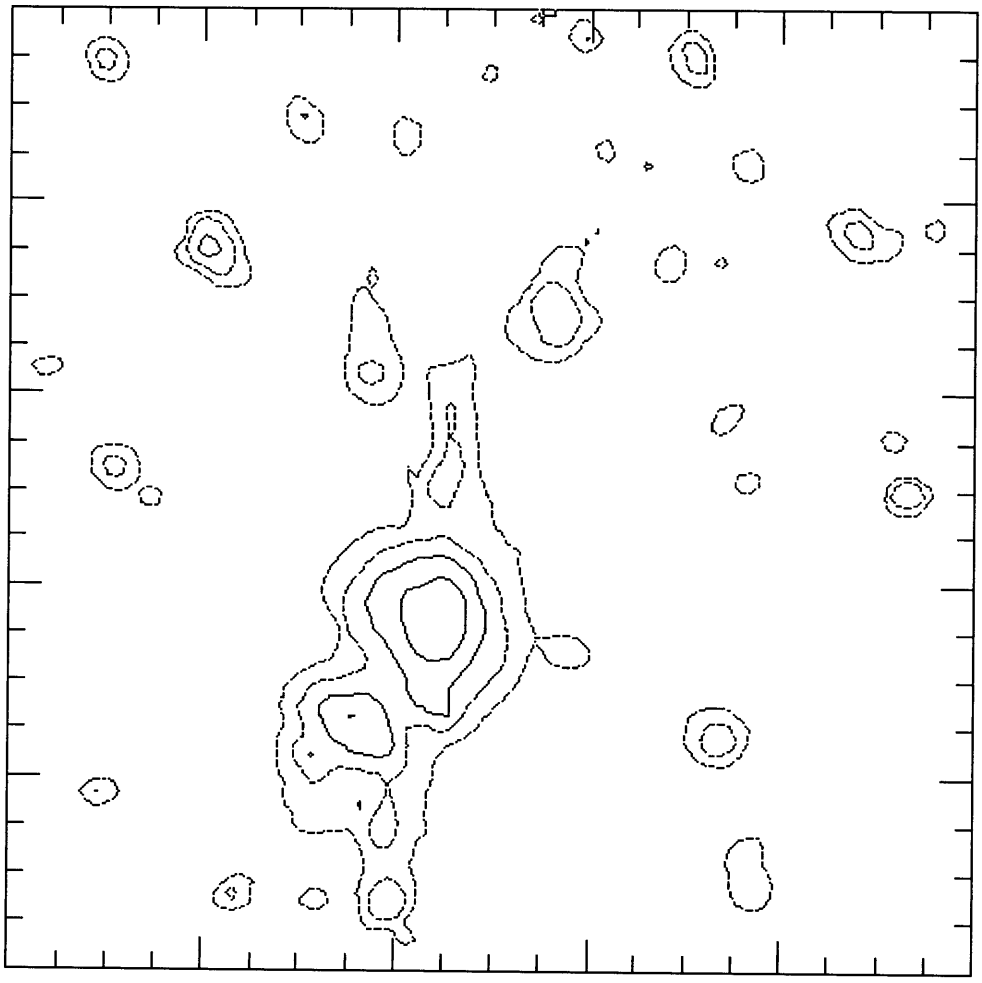

Figure A-12: Panel G.

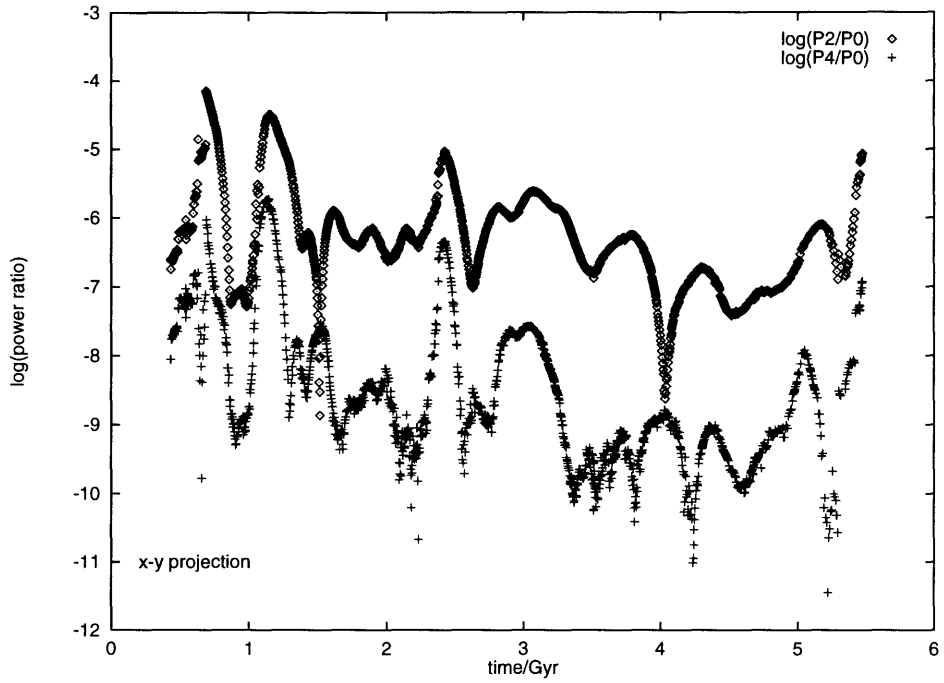

Figure A-13: Power ratios P_2/P_0 (diamonds) and P_4/P_0 (crosses) versus time for the $x-y$ projection.

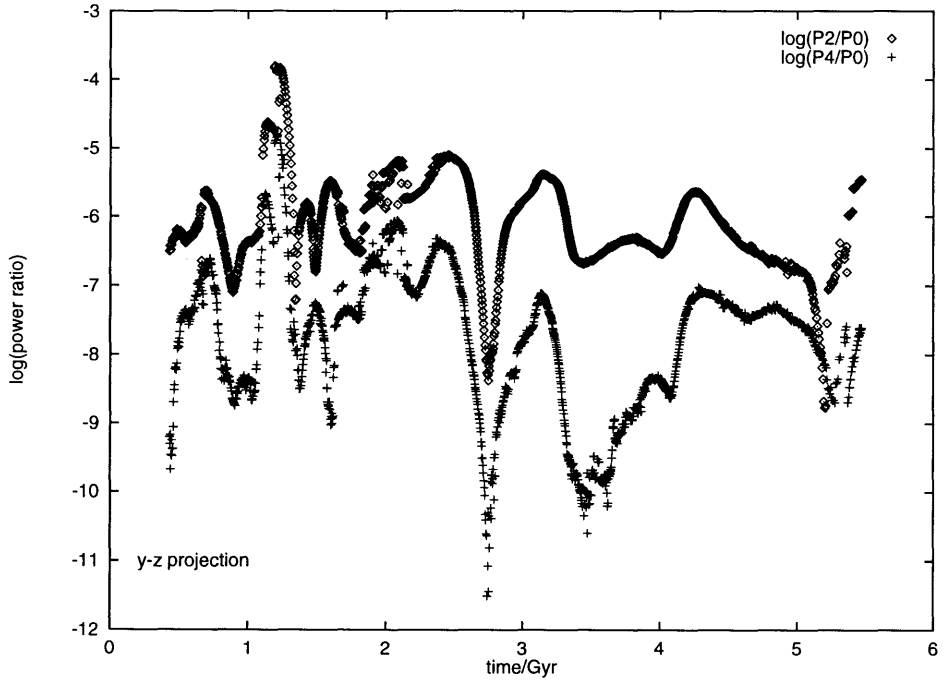

Figure A-14: Power ratios P_2/P_0 (diamonds) and P_4/P_0 (crosses) versus time for the $y-z$ projection.

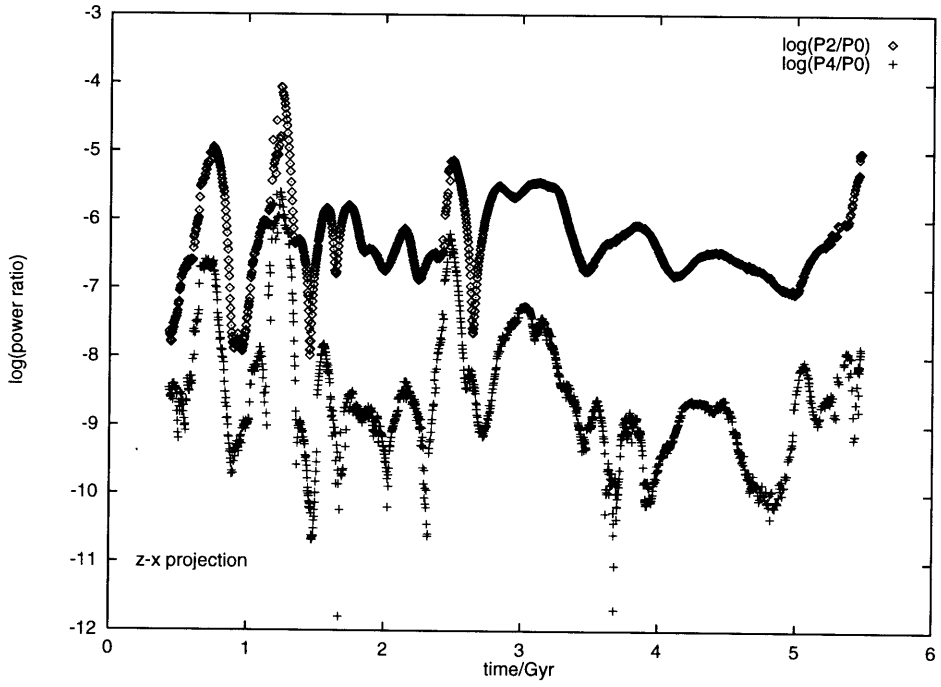

Figure A-15: Power ratios P_2/P_0 (diamonds) and P_4/P_0 (crosses) versus time for the $z-x$ projection.

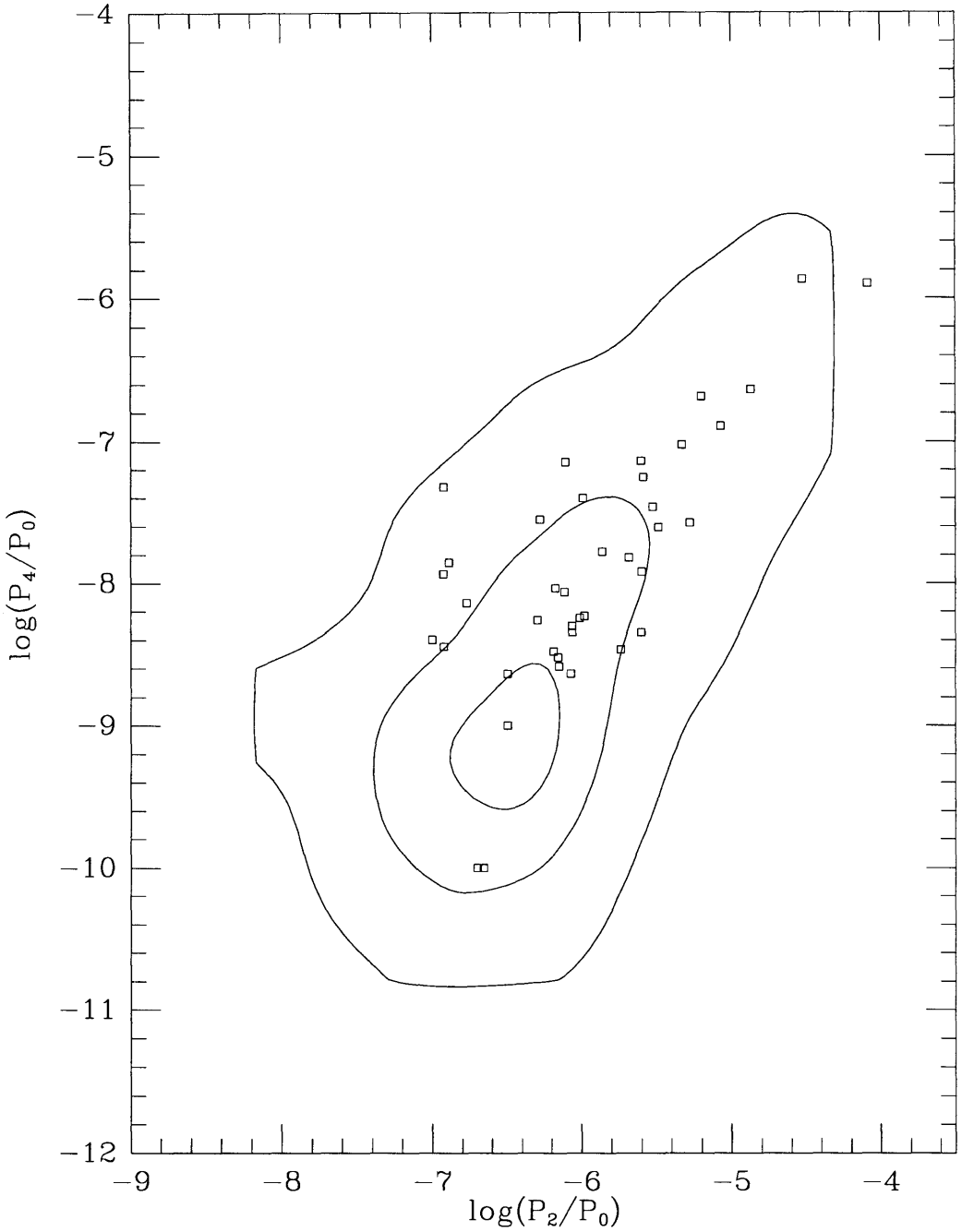

Figure A-16: Occupation probabability in the P_2/P_4 plane. Countours are at 1, 10, 20 and 30. The cluster spends a factor of 30 more time near the 30 contour than near the 1 contour. The region outside the level 1 contour is effectively never occupied. Points are for the Buote & Tsai (1996) Rosat clusters.

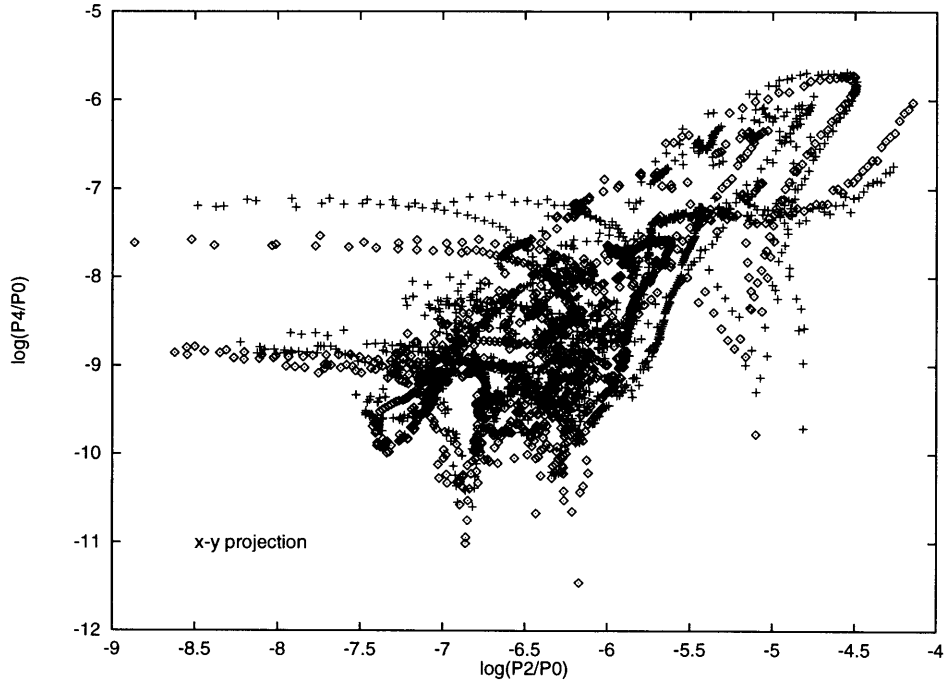

Figure A-17: Power ratio trajectory computed for the X-ray surface brightness (diamonds) and under the isothermal assumption (crosses).

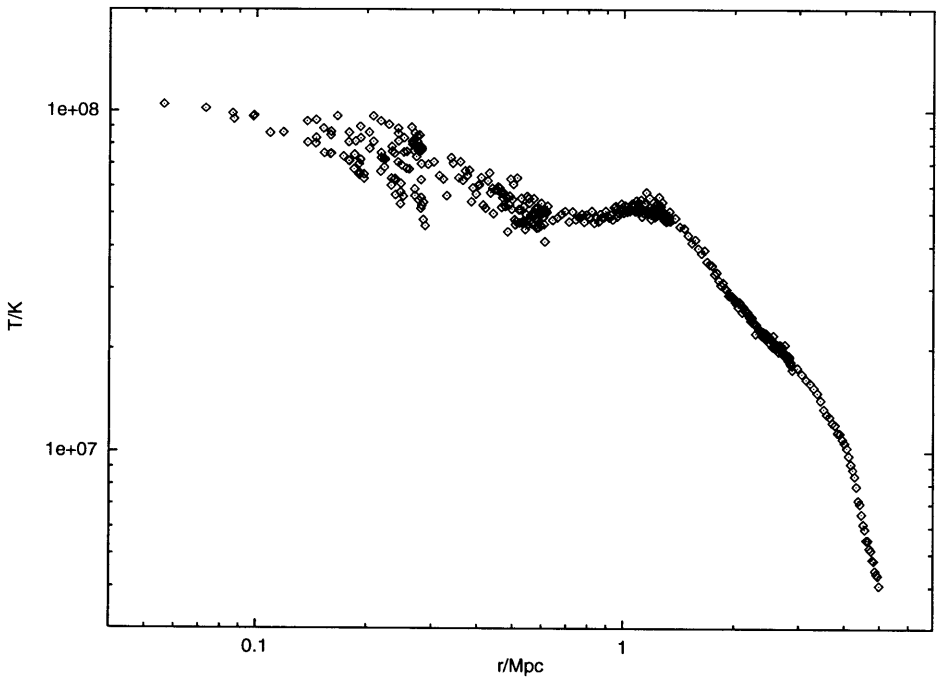

Figure A-18: Spherically averaged gas temperature profile.

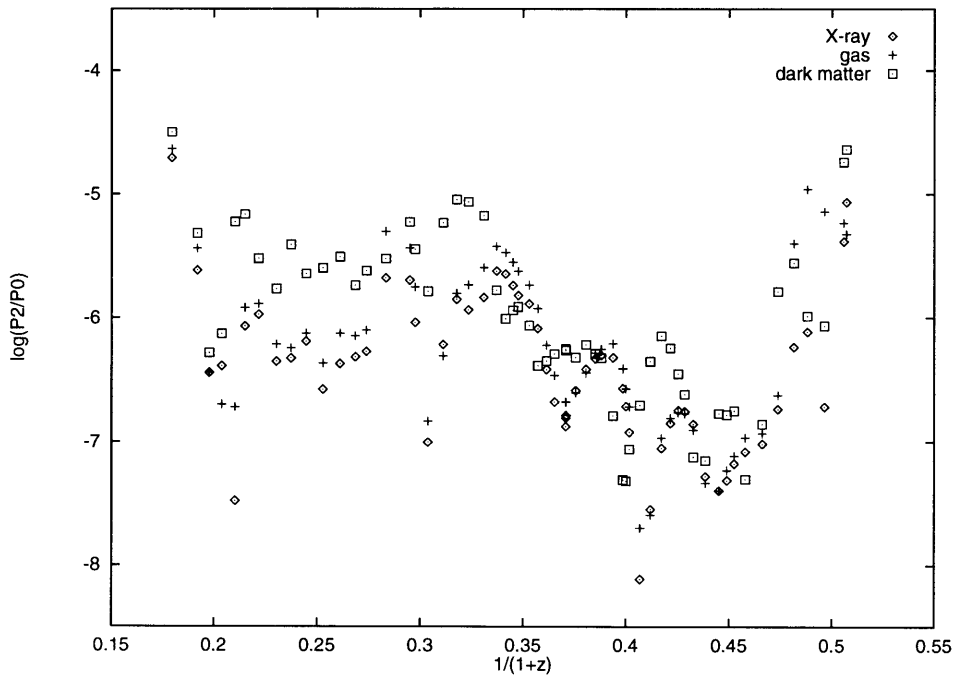

Figure A-19: P_2/P_0 versus expansion factor, with the power ratio calculated from the X-ray surface brightness (diamonds), the square of the gas density (crosses) and the square of the dark matter density (squares).

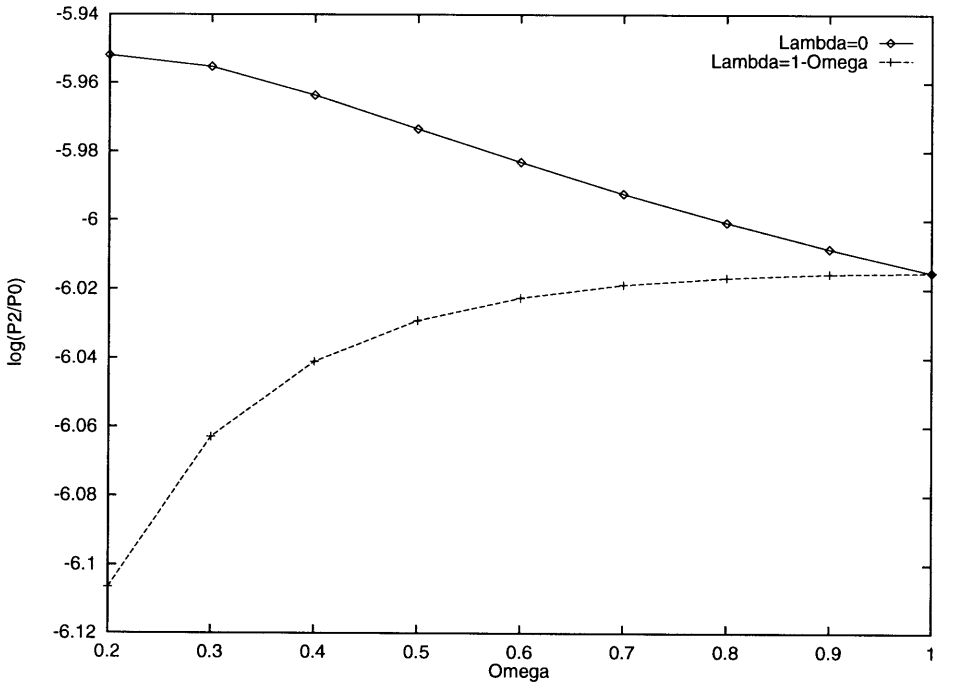

Figure A-20: Dependence of predicted mean power ratio P_2/P_0 on the mean density Ω, for both open and flat models with cosmological constant.

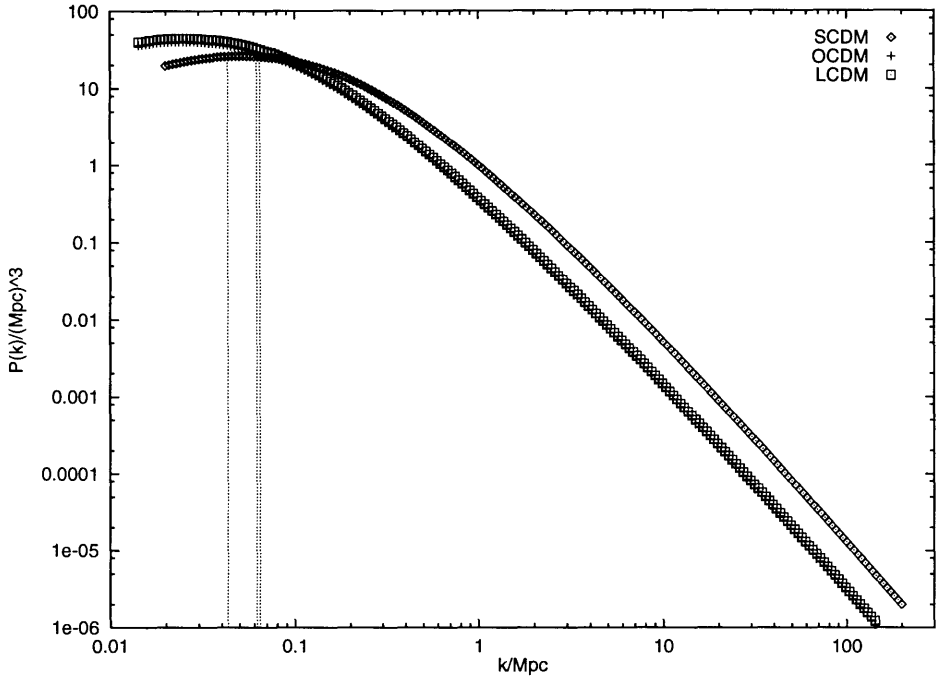

Figure A-21: Power spectra of initial density fluctuations $P(k)$ plotted vs. wavenumber k for the SCDM (diamonds), OCDM (crosses), and LCDM (squares) models. The vertical marks indicate the scale $k = 1/R_{\rm TH}$ for the halo of mass $M_{\rm low}$, where $M_{\rm low} = 4/3\pi R_{\rm TH}^3 \bar{\rho}$. From left, these marks correspond to SCDM, LCDM and OCDM.